HHS Public Access

Author manuscript

Neuron. Author manuscript; available in PMC 2023 July 03.

Published in final edited form as:

Neuron. 2022 December 21; 110(24): 4090–4107.e11. doi:10.1016/j.neuron.2022.09.021.

Motor neurons use push-pull signals to direct vascular remodeling critical for their connectivity

Luis F. Martins[1,4], **Ilaria Brambilla**[1], **Alessia Motta**[1], **Stefano de Pretis**[1,3], **Ganesh Parameshwar Bhat**[1], **Aurora Badaloni**[1], **Chiara Malpighi**[1], **Neal D. Amin**[2,9], **Fumiyasu Imai**[6,7], **Ramiro D. Almeida**[4,5], **Yutaka Yoshida**[6,7,8], **Samuel L. Pfaff**[2,*], **Dario Bonanomi**[1,10,*]

[1]San Raffaele Scientific Institute, Division of Neuroscience, via Olgettina 60, 20132 Milan, Italy

[2]Gene Expression Laboratory, Salk Institute for Biological Studies, 10010 North Torrey Pines, La Jolla, CA 92037, USA

[3]Center for Omics Sciences, San Raffaele Scientific Institute, Milan, Italy

[4]CNC, Center for Neuroscience and Cell Biology, University of Coimbra, Coimbra 3004-504, Portugal

[5]iBiMED - Institute of Biomedicine, Department of Medical Sciences, University of Aveiro, Aveiro 3810-193, Portugal

[6]Burke Neurological Institute, White Plains, NY 10605, USA

[7]Brain and Mind Research Institute, Weill Cornell Medicine, New York, NY 10065, USA

[8]Neural Circuit Unit, Okinawa Institute of Science and Technology Graduate University, Okinawa, Japan

[9]Present address: Department of Psychiatry and Behavioral Sciences, Stanford University, Stanford, CA 94305, USA

[10]Lead contact

SUMMARY

The nervous system requires metabolites and oxygen supplied by the neurovascular network, but this necessitates close apposition of neurons and endothelial cells. We find motor neurons attract vessels with long-range VEGF signaling, but endothelial cells in the axonal pathway are an obstacle for establishing connections with muscles. It is unclear how this paradoxical interference from heterotypic neurovascular contacts is averted. Through a mouse mutagenesis screen, we

*Correspondence: pfaff@salk.edu (S.L.P.), bonanomi.dario@hsr.it (D.B.).

AUTHOR CONTRIBUTIONS

D.B. designed and supervised the study, collected data, and wrote the manuscript. S.L.P. supervised the mouse mutagenesis screen and revised the manuscript. L.F.M. collected and analyzed data with the help of I.B., A.M., G.P.B., A.B., and C.M. F.I. conducted ligand-binding assay. N.D.A. generated scRNA-seq data. S.d.P. performed computational analysis. R.D.A. and Y.Y. provided samples, reagents, and critical comments.

SUPPLEMENTAL INFORMATION

Supplemental information can be found online at https://doi.org/10.1016/j.neuron.2022.09.021.

DECLARATION OF INTERESTS

The authors declare no competing interests.

show that Plexin-D1 receptor is required in endothelial cells for development of neuromuscular connectivity. Motor neurons release Sema3C to elicit short-range repulsion via Plexin-D1, thus displacing endothelial cells that obstruct axon growth. When this signaling pathway is disrupted, epaxial motor neurons are blocked from reaching their muscle targets and concomitantly vascular patterning in the spinal cord is altered. Thus, an integrative system of opposing push-pull cues ensures detrimental axon-endothelial encounters are avoided while enabling vascularization within the nervous system and along peripheral nerves.

Graphical Abstract

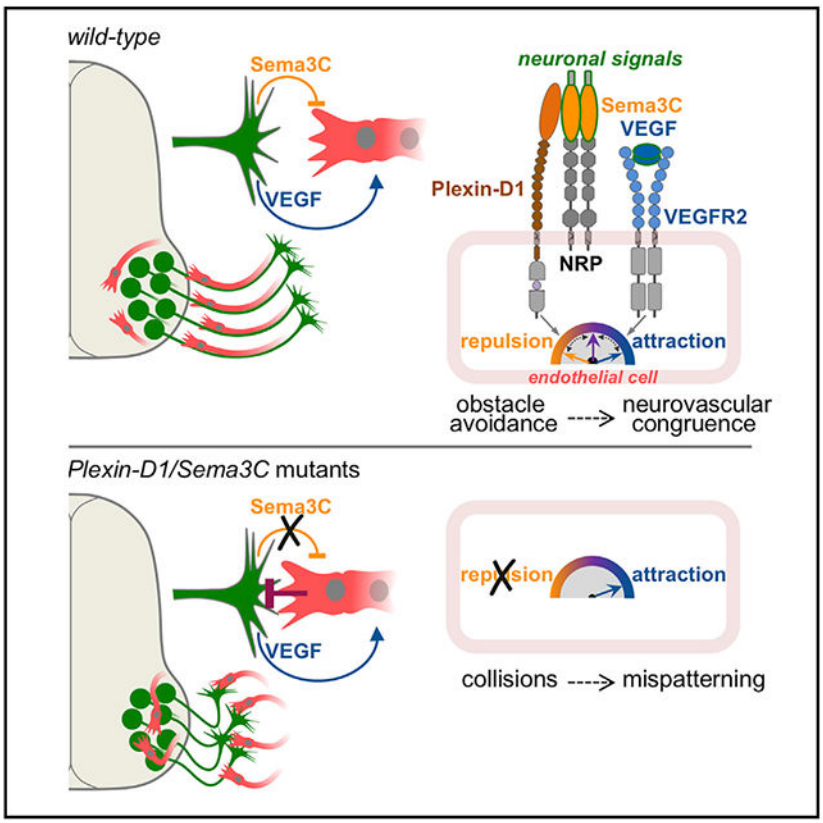

In brief

Axons navigate complex environments where unwanted encounters with other cells might hinder their course. Martins et al. identify a selective obstacle-removal pathway based on short-range Sema3C/Plexin-D1 repulsive signaling that motor neurons employ to evade collisions with blood vessels while enabling assembly of interdependent neurovascular networks through attraction of endothelial cells.

INTRODUCTION

During embryonic development, neurons project through dense and heterogeneous environments guided by chemical and mechanical cues (Franze et al., 2013; Kolodkin and Tessier-Lavigne, 2011). Owing to concomitance of tissue morphogenesis and innervation,

axons are confronted with a noisy and changing terrain, where true guideposts may be masked, and obstacles—in the forms of physical barriers or unwanted cell-cell contacts—interfere with pathfinding (Dodd and Jessell, 1988; Klose and Bentley, 1989; Tosney and Landmesser, 1985a). Despite these complications, neurons rarely make projection errors indicating that safeguard mechanisms are in place (Landmesser, 1978). This is in part achieved through cell-intrinsic switches that gate receptor signaling limiting detection to relevant cues (Bai et al., 2011; Bonanomi et al., 2019; Zang et al., 2021). In addition, neuronal growth cones form invasive structures and release matrix-degrading proteases to remove some of the physical constraints in tissues (Nichols and Smith, 2019; Santiago-Medina et al., 2015). However, while the instructive effect of tissue-derived signals on neuronal guidance have been studied in detail, much less is known on how axons affect the behavior of cells along their projection paths.

Coordinated interactions between axons and their cellular environment are manifested in the formation of apposed and interdependent neurovascular networks (Tam and Watts, 2010). This process begins in the embryo, when nerves and vessels attract each other through release of chemotropic factors or, alternatively, display independent but correlated responses to guidance cues (Carmeliet and Tessier-Lavigne, 2005; Eichmann and Brunet, 2014; James and Mukouyama, 2011). The significant overlap between periods of axon growth and angiogenesis suggests that the two processes must be harmonized to prevent interference (Erskine et al., 2017; James et al., 2009). Nonetheless, current models based on the principle of “one patterns the other” (Andreone et al., 2015), in which pre-established neural or vascular systems serve as template, do not resolve how axons negotiate their encounters with vessels when both are simultaneously engaged in pathfinding.

Navigating crowded tissues is particularly challenging for pioneer axons that set new routes in the absence of preexisting nerve tracts. This is the case for spinal motor neurons (MNs) that are the first to project through the mesenchymal environment, thereby laying down the basic pattern of peripheral nerve trajectories. MN subtypes that innervate functionally related muscle groups cluster together (Jessell, 2000). All motor axons travel initially in a common nerve until each subtype branches-off at defined choice-points to follow specific routes toward the appropriate target (Bonanomi, 2019; Tosney and Landmesser, 1985a). An evolutionarily conserved set of medial motor column (MMC) neurons with epaxial projections controls locomotion in limbless vertebrates and body posture in tetrapods (D’Elia and Dasen, 2018; Fetcho, 1987), while distinct MN subtypes that evolved from this ancestral population contact hypaxial or limb muscles.

Taking advantage of the topographic organization of MN projections, we conducted a mouse forward genetic screen to isolate factors involved in neuromuscular connectivity. This analysis led to identification of the *Drake* mutant line harboring a missense mutation in *Plexin-D1*, a transmembrane receptor for Semaphorins. Plexin-D1 is best known as high-affinity receptor for Sema3E (Gu et al., 2005). The interaction is direct, unlike other class 3 secreted Semaphorins that bind to Neuropilins (NRPs) and rely on Plexins as signal-transducing co-receptors. By mediating Sema3E signaling, Plexin-D1 regulates vascular patterning, axon guidance, synapse formation, and metastasis (Oh and Gu, 2013). Here, through the study of *Drake* mutants with loss of function of *Plexin-D1*, we reveal

an unexpected co-dependency between motor axons and vessels during pathfinding and show that neurons repurpose guidance signals to prevent detrimental interactions with endothelial cells (ECs). This crosstalk reconciles the opposing requirement for neurovascular congruency with the simultaneous need to overcome cellular barriers along axon projection paths.

RESULTS

An ENU-induced allele of *Plexin-D1* causes cell-type-specific motor axon guidance defects

We designed an N-ethyl-N-nitrosourea (ENU)-mutagenesis mouse screen to identify recessive alleles that affect neuromuscular connectivity (Lewcock et al., 2007). On this basis, we isolated the mutant line *Drake*, which displayed MN projection defects characterized by large ectopic axon fascicles just outside the spinal cord (SC) (Figures 1A-1F and S1A-S1D). At all affected spinal roots, the presence of aberrant bundles was invariably associated with severe disruption of epaxial nerves, which were markedly thinner or absent (asterisks in Figures 1A-1D and S1A-S1D). In contrast, nerves supplying muscles in the limb or body wall were normal (Figure S1E; data not shown). Selective depletion of epaxial projections suggested that the ectopic proximal bundles were formed mostly—or completely—by MMC-subtype motor axons that had stalled shortly after exiting the SC (Figure 1G). Thus, the *Drake* mutation specifically affects targeting of a discrete set of axial MNs.

RNA sequencing (RNA-seq) of *Drake* mutants identified an A>T transversion in the first exon of *Plxnd1* (Figures 1H and 1I). *Drake* embryos were homozygous for the mutation that led to C116S substitution in the extracellular ligand-binding (Sema) domain of Plexin-D1. Cys-116 is part of a conserved set of cysteines that form disulfide bridges stabilizing the structure of the Sema domain (Antipenko et al., 2003; Love et al., 2003; Figures 1H, 1J, and S1G). Plexin-D1 transcript and protein levels were unchanged in *Drake* (*Plxnd1*$^{C116S/C116S}$) embryos (Figures 1K and S1H) but surface targeting of Plexin-D1^{C116S} was impaired (Figures S1I-S1L). The mutation abolished binding of Sema3E to Plexin-D1 (Figures 1L and 1M) and prevented induction of cell collapse (Figures 1N and 1O; Gu et al., 2005). Taken together, *Plxnd1*^{C116S} is likely a severe loss-of-function allele of Plexin-D1 that abolishes receptor activity by interfering with ligand-binding, owing to altered folding and/or impaired membrane targeting. *Plxnd1* knockout (KO) embryos exhibited motor axon defects similar to *Drake* mutants (Figure S1F), further indicating that the inactivating C116S mutation was responsible for the phenotypes.

Endothelial Plexin-D1 is required for motor neuron targeting and controls axon-vessel interactions

Plexin-D1 was enriched in ECs in both the SC and peripheral tissues but was undetectable in MNs in E10.5–E12.5 embryos (Figures 2A, 2B, S2A, S2B, and S6A). This distribution suggested that axon defects observed in *Plxnd1* mutants might be non-cell-autonomous, caused by impaired Plexin-D1 activity in blood vessels rather than MNs. To test this possibility, we generated compound mutant embryos carrying one copy of *Plxnd1*^{C116S} and one *Plxnd1* “floxed” allele deleted from either ECs with *Tek*^{EC}*::Cre*, or from MNs

with *Olig2^{MN}::Cre*. While motor projections were normal in embryos lacking *Plxnd1* in MNs, gene deletion in ECs resulted in axon guidance defects closely resembling those found in *Drake* and *Plxnd1* KO embryos (Figures 2C-2F and S2C-S2E). The phenotype was fully penetrant, detected in all homozygous *Drake* or *Plxnd1*-null mutants and *Tek^{EC}::Cre;Plxnd1$^{C116/fl}$* embryos but never in hemizygotes. A scoring system integrating the number of ectopic bundles and affected ventral roots (VRs), quantified in *ISL^{MN}::fGFP* embryo whole mounts, confirmed that the severity of the phenotype was similar between *Drake, Plxnd1$^{-/-}$* and *Tek^{EC}::Cre;Plxnd1$^{C116/fl}$* embryos (Figure 2G). In addition, lack of complementation between *Plxnd1^{C116S}* and KO alleles in compound hemizygotes demonstrated that *Drake* is a loss-of-function mutant of *Plxnd1*. These findings revealed a requirement for Plexin-D1 in ECs for targeting of MMC axons to epaxial muscles.

In control embryos, MMC axons grew through the VR populated with vessels (Figure 2H), whereas the abnormal axon bundles of *Plxnd1* mutants were bordered by misplaced ECs (Figure 2I, arrowheads). Thus, while MMC axons normally extended through dispersed ECs avoiding direct contact (Figures 2J, 2J′, 2L, and 2N), their projection in mutant embryos was obstructed by an ectopic “endothelial barrier” positioned at the choice point for epaxial innervation (Figures 2K, 2K′, 2M, and 2O). In contrast, targeting of MNs supplying limb muscles (lateral MC [LMC]) or intercostal nerves (hypaxial MC [HMC]) was preserved despite close encounters with ECs (Figures S2F-S2M′). At lumbar level, the initial course of limb-innervating axons was devoid of vessels, whereas the first MMC axons veering from the common nerve intersected ECs abutting the meningeal vascular plexus, which had begun to enwrap the proximal nerve segment (Figures 2P-2Q′ and S2N-S2Q′). Nevertheless, MMC axons bypassed vessels in control embryos (Figures 2R, 2R′, S2R, and S2R′), while in *Plxnd1* mutants they collided with EC clusters (Figure 2S, 2S′, and S2S-S2T′). These studies reveal a choreographed progression of neurovascular association within the VR and indicate that the interactions between MMC neurons and ECs require *Plxnd1* signaling to ensure axial muscle innervation (Figure 2T).

Motor axons define vascular topography at the ventral root

Given the correlated development of axons and vessels at the VR, we asked whether motor nerves contributed to the spatial organization of the vascular network in this region. MNs were genetically ablated before they extended axons from the SC by combining *Olig2^{MN}::Cre*, which is active in MN progenitors, with conditional diphtheria toxin A (DTA) allele (*DTA^{LSL}*). Lack of motor projections dramatically affected vascular patterning. In *Olig2^{MN}::Cre*; *DTA^{LSL}* embryos, vessels failed to align precisely with spared sensory fibers and coalesced around motor exit points (Figures 3A-3D′ and S3A-S3C). The organization of the vascular network around the proximal motor nerve segment, characterized by vascular “rings” traversed by axons, collapsed in absence of motor nerves (Figures 3E-3G). Therefore, vascular topography of the VR zone is shaped by motor axons that co-develop with vessels establishing matching patterns.

Plexin-D1 controls vascularization of the motor columns

In addition to disrupted axon-endothelial interactions in the periphery, *Plxnd1* mutant embryos displayed severe defects in vascular patterning within the SC. Specifically, the

MCs, which at early embryonic stages are devoid of blood vessels (Himmels et al., 2017; James et al., 2009), became abnormally vascularized in mutants. Vessels normally formed half loops extending at the border of the MCs (Figures 3H and 3H′) and invaded this region only after E12.5 (see e.g., Figure 3A). Their intraspinal course depended on MC integrity, since vascularization was impaired following MN ablation (Figures S3D-S3E′). The stereotypical vascular pattern observed in control embryos was profoundly affected in *Plxnd1*^{C116S} and *Plxnd1*-null homozygotes, as well as in embryos carrying EC-specific deletion of *Plxnd1*. Mutants displayed abnormal vessel ingression into the MC that resulted in significant increase in vascular density within this domain (Figures 3I-3L) accompanied by excessive filopodial sprouting indicative of deregulated angiogenesis (Figures S3F-S3G″). In contrast, vascularization of the dorsal SC was unaffected (Figures 3M, S3H, and S3I). Vascular invasion of the MC was observed at all segmental levels in *Plxnd1* mutants (Figures S3L-S3R) and was concomitant with the first appearance of ectopic axon-endothelial bundles in the periphery at ~E11.5 (Figures S2S-S2T′). However, while axonal defects were restricted to MMC neurons, vessels spread irregularly throughout the MC, intermingling with the cell bodies of different MN subtypes (Figures S3I and S3L-S3Q′). Despite these changes, the number and columnar clustering of MNs, including MMC neurons, were not altered (Figures S3J-S3Q′). These results suggest that loss of Plexin-D1 in ECs impairs detection of ventral SC-derived signals, leading to premature and unrestrained vascular invasion of MNs (Figure 3N).

Motor axons repel endothelial cells through Plexin-D1

Our observations are consistent with direct MN-endothelial signaling mediated by Plexin-D1 but other cell types coexisting in the same territory might also contribute (Suter and Jaworski, 2019). To test unambiguously the interactions between MNs and ECs, we established a co-culture system in which human umbilical vein ECs (HUVECs) were seeded on top of mouse MN explants before axons had begun to extend. ECs initially adhered near the explant but progressively withdrew from the advancing axons, avoiding overlap, and eventually (~15 h later) formed a monolayer aligned with the axonal front (Figures 4A, 4B top, 4D, 4D′, and S4A-S4C′; Videos S1, S2, S3, and S4). EC death was not observed during this process. This opposing behavior indicated that ECs were repelled by motor axons, resulting in cell-free area that was measured to quantify the extent of repulsion (Figure 4C). The aversive signal was mostly associated with axons rather than cell bodies in the explant, since co-cultures grown on low-laminin substrate to prevent axon extension-while allowing EC adhesion/migration—displayed limited repulsion (Figures 4J, S4H, and S4H′). EC repulsion was strongly inhibited when *Plxnd1* was knocked down (KD) in HUVECs prior to co-culture with motor explants (Figures 4B bottom, 4C, 4F, 4F′, 4J, S5L, and S5M; Videos S5 and S6), and this effect was recapitulated by treatment with a blocking antibody against Plexin-D1 (Figures 4J and S4I-S4J′). Cells lacking constitutive expression of *Plxnd1*, such as fibroblasts, were not repelled (Figures 4J and S4L). Therefore, Plexin-D1 is needed in ECs to detect repulsive signal(s) associated with motor axons. The repulsive activity was conserved in motor explants from chick embryos and also in this case depended on Plexin-D1 in ECs (Figures 4H, 4I, and 4K). Of note, *Plxnd1* KD did not affect the rate of EC proliferation and migration per se (Figures 5M and S4Q).

Motor axons rarely overshot the endothelial boundary, suggesting that ECs provided an unfavorable substrate (Figures 4D and 4E). Indeed, axon extension was reduced in co-cultures compared with explants grown alone (Figures 4L and S4G) and growth cones reaching the endothelial interface frequently exhibited a "collapsed" morphology indicative of avoidance behavior (Figure S4E). Axon growth was further impaired when explants were confronted with ECs silenced for *Plxnd1*, which they could not efficiently repel (Figure 4L). In this condition, axons were shorter, hyperfasciculated, and twisted at the interface with ECs; when they extended incoherently on the cell monolayer their growth cones were often abnormally enlarged (Figures 4G, S4D, and S4F). Thus, ECs appear to express non-permissive/repulsive factors that counter axon growth. These signals are likely to function at short range and/or in contact-dependent manner since motor axon elongation was not affected by HUVEC-conditioned media (Figure 4M).

We next asked how ECs responded when co-cultured with other populations of spinal neurons that, unlike MNs, project their axons exclusively within the central nervous system (CNS). Dorsal SC explants containing commissural interneurons were inefficient at repelling HUVECs, and their limited repulsive activity was independent of Plexin-D1 (Figures S4N-S4P). However, as for MNs, axon growth from dorsal explants was reduced in the presence of ECs (Figure S4N, compare with S4M). Likewise, SC interneurons inadvertently included within MN explants were unable to repel ECs but avoided crossing their boundary (Figure S4C′).

Taken together, these *in vitro* data indicate that signals from MNs repel ECs through Plexin-D1, and conversely that ECs express factors that hinder axon growth. The effect of disrupted balance between these opposing activities unmasked by *Plxnd1* silencing in co-cultures is reminiscent of the phenotype observed in *Plxdn1* mutant embryos, characterized by axons stalling against an "endothelial barrier."

Motor neuron-derived Sema3C triggers endothelial cell repulsion via Plexin-D1/Neuropilin receptors

To identify relevant Plexin-D1 ligands that would mediate the repulsive effect of MNs on ECs, we first surveyed expression of Semaphorins in RNA-seq data of MNs (Bonanomi et al., 2019). MNs expressed members of the family but surprisingly lacked Sema3E—the canonical Plexin-D1 ligand—which was undetectable when phenotypes developed in *Plxnd1* mutants (Figures 5A and S5B). Additional ligands for Plexin-D1 have been proposed (Feiner et al., 2001; Gitler et al., 2004; Hamm et al., 2016; Liu et al., 2016; Torres-Vázquez et al., 2004; Toyofuku et al., 2007). Among these, *Sema3C* was expressed at high levels in MNs (Figures 5A, 5B, S5A, and S5E) and was detected in all MN subtypes along the rostrocaudal axis, with relative enrichment in the MMC (Figure S6D; data not shown). Next, we tested whether KO embryos for candidate Plexin-D1 ligands displayed the phenotypes observed in *Plxnd1* mutants. In addition to *Sema3E* and *Sema3C* mutants, we analyzed embryos KO for *Sema4A*—a Plexin-D1 ligand expressed in MNs (Figure 5A; Toyofuku et al., 2007). Loss of *Sema3C* resulted in abnormal vascular ingression into the MC, similar to *Plxnd1* KO, whereas vessels remained excluded from this region in $Sema3E^{-/-}$ and $Sema4A^{-/-}$ embryos (Figures 5C-5E). However, vascular defects were less pronounced in $Sema3C^{-/-}$

compared with *Plxnd1* mutants (Figure 5E compare with Figure 3L). Next, *ISL^{MN}::fGFP* was crossed into *Sema3E, Sema3C*, and *Sema4A* KO mice to analyze motor projections. Axon targeting was normal in *Sema3E$^{-/-}$* and *Sema4A$^{-/-}$* embryos (Figures 5F-5H and 5J) despite disorganization of the intersomitic vasculature in *Sema3E* mutants (Figures S5C and S5D; Gu et al., 2005). In contrast, ~60% of *Sema3C$^{-/-}$* embryos displayed motor axon defects resembling the phenotype of *Plxnd1* mutants, albeit with reduced severity (Figures 5I-5K). Thus, loss of *Sema3C* causes vascular and axon guidance errors that phenocopy *Plxnd1* mutation, suggesting that Sema3C signals via Plexin-D1 to regulate MN-EC interactions.

The incomplete penetrance of *Sema3C* KO might indicate compensation from other Semaphorins (Figures 5A, S5A, and S5F). We reasoned that examining directly the interaction between axons and ECs *in vitro* might reveal a requirement partially masked *in vivo*. A “scratch assay” showed that Sema3C inhibited EC migration through Plexin-D1 (Figures 5L and 5M). *Sema3E$^{-/-}$* motor explants repelled ECs, whereas this response was hindered with explants from either *Sema3C* heterozygous (~20% decrease) or KO (~60% decrease) embryos (Figures 5N-5P, S5J, and S5K). Inefficient repulsion in *Sema3C$^{+/-}$* co-cultures suggests that ECs are sensitive to intermediate decrease in Sema3C doses (Figures S5G and S5H). Motor axon extension was normal in *Sema3C* KO explants, indicating that impaired EC repulsion was not due to defective axon growth (Figure S5I). In conclusion, Sema3C accounts for a large portion of the repulsive activity of motor axons toward ECs detected in co-cultures.

Sema3C binds to Neuropilin-1 (NRP1) and Neuropilin-2 (NRP2) while Plexin-D1 functions as a co-receptor (Chen et al., 1998; Christie et al., 2021). Besides enabling signaling, Plexin-D1 enhanced binding of Sema3C to NRP (Gitler et al., 2004) and the C116S (*Drake*) mutation reduced this effect (Figures S5N and S5O). HUVECs with KD of either *Plxnd1*, *Nrp1*, or *Nrp2* showed impaired repulsion from Sema3C released by HEK cells, confirming that while Plexin-D1 mediates Sema3E signaling directly, it relies on NRPs to transduce Sema3C signal (Figures 5Q and S5P). Consistent with this requirement, either *Nrp1* or *Nrp2* KD in HUVECs compromised repulsion from motor explants (Figures 5R-5U). The magnitude of the decrease was less pronounced than after *Plxnd1* silencing, possibly due to redundancy and compensation between NRPs (Figure S5M) (Chen et al., 1998; Gitler et al., 2004; Gu et al., 2003; Plein et al., 2015). Therefore, Plexin-D1/NRP complexes are required in ECs to detect repulsive MN signals. To test sufficiency, we generated HEK cell lines expressing Plexin-D1 alone or together with either NRP1 or NRP2 and cultured them with motor explants. Naive HEKs, which lack *Plxnd1, Nrp1*, and *Nrp2*, did not respond to either Sema3E or Sema3C and were not repelled by motor axons (Figures 5V, S5Q, and S5R; data not shown). In contrast, HEKs stably transfected with these receptors responded predictably to Sema3E (HEK-Plxnd1) and Sema3C (HEK-Plxnd1/NRP1 or Plxnd1/NRP2) (Figures S5Q and S5R). When co-cultured with motor explants, HEKs expressing Plexin-D1 alone were not repelled, while those co-expressing Plexin-D1 and NRP gained repulsion (Figures 5W-5Z). Together, these studies show that Sema3C derived from MNs repels ECs through Plexin-D1/NRP complexes.

In silico screening of signaling interactions governing motor-endothelial crosstalk

Communication between MNs and ECs is impaired by loss of Plexin-D1. To gain insights into the underlying mechanisms, ECs from the SC and surrounding meninges were sorted from *Plxnd1*$^{-/-}$ embryos and control littermates based on *Kdr*^{EC}*::Cherry* reporter signal and analyzed by RNA-seq (Figure 6A). The meningeal sheath covering the SC and VRs was included in order to capture ECs associated with the proximal nerve region where abnormal axon-vessel interactions develop in mutants. From the same embryos, we sorted and sequenced *ISL*^{MN}*::fGFP*$^{+}$ MNs to identify secondary (non-cell autonomous) transcriptional changes resulting from loss of *Plxnd1* in ECs (Figure 6A). EC profiling of *Plxnd1* mutants identified moderate deregulation in genes involved in vascular development (Figures 6B and 6C; Table S1). Although MNs purified in parallel to ECs did not express *Plxnd1* (Figure S6A), in mutant embryos, they displayed changes in a restricted set of genes related to axon guidance and cell-cell interactions (Figures 6D and 6E; Table S1). *Sema3C* and vascular endothelial growth factor (*Vegfa*) increased, suggesting that MNs react to perturbations resulting from loss of vascular *Plxnd1* by modulating genes that signal directly to ECs. Expression-weighted cell-type enrichment (EWCE) showed that genes upregulated in *Plxnd1*$^{-/-}$ MNs were overrepresented in a MMC subset identified by single-cell RNA-seq (scRNA-seq) (Amin et al., 2021; Figures 6F, S6B, and S6C). Therefore, a significant degree of gene expression changes that developed in MNs as a result of *Plxnd1* loss in the endothelium were confined to epaxial MNs, whose axons interacted abnormally with vessels in mutants.

Robust signaling was inferred between MMC neurons and ECs on the basis of expression of matched ligand-receptor genes, which were associated with neuronal guidance and vascular morphogenesis pathways (Figures 6G and 6H; Table S3). Among the strongest predicted interactions, we detected MMC-derived Sema3C coupled to endothelial Plexin-D1, NRP1, and NRP2 (Figures 6I and S6D; Table S4). MMC neurons expressed several additional factors that could either inhibit (*Sema3A, Slit2*, and *EphrinB2*) or promote (*Vegfa* and *pleiotrophin*) angiogenesis (Figures 6I and S6D; Table S4). Conversely, EC expressed signals that might influence axon growth, including adhesive ECM molecules (collagens, laminins, and perlecan/*HSPG2*) or repulsive factors such as Semaphorins (*Sema6A* and *Sema6D*) and ephrins (*Efna1, Efna2, Efnb1*, and *Efnb2*) (Figures 6J and S6E; Table S4). All EC receptors and ligands predicted to be involved in signaling with MMC neurons (Figures 6I and 6J) were detected in the intraspinal and meningeal endothelium, often displaying differential expression (Figures 6K, 6L, and S6F-S6J; Table S5), and were therefore present in vessels within the regions where neurovascular defects arise in *Plxnd1* mutants (i.e., the SC and VR).

Plexin-D1 antagonizes VEGF to control motor neuron-endothelial interactions

Aberrant MC vascularization in *Plxnd1* mutants suggests unmasking of attractive signals associated with MNs. The release of EC attractants from MNs was demonstrated by enhanced migration of HUVECs toward MN-conditioned media (Figures 7A, 7B, and 7D). Treatment with a neutralizing anti-VEGF164 antibody abolished this response (Figures 7C and 7D) but did not interfere with chemoattraction per se (Figure S7C). Thus, VEGF-A secreted from MNs (Figures S7A-S7B′) (Himmels et al., 2017; Mukouyama et al., 2005)

attracts ECs at long range, overriding the repulsive signals from motor explants revealed in co-cultures. Since *Plxnd1* KD did not perturb EC migration toward MN-conditioned media or recombinant VEGF, the two pathways appear to operate independently (Figures S7D-S7I). To address how antagonistic neuronal signals were integrated by ECs, we treated motor-endothelial co-cultures with anti-VEGF antibody. VEGF depletion partially restored repulsion of *Plxnd1*-KD HUVECs from motor explants (Figures 7E-7I′) and concomitantly improved axon growth (Figures 7I versus 7H). These results suggest that EC attraction toward MNs in the absence of efficient repulsion interferes with nerve projection. When attraction was attenuated by anti-VEGF treatment, Plexin-D1-independent repulsive signals associated with MNs could partially rescue axon-endothelial interactions.

This model was tested *in vivo* by generating *Plxnd1* KO embryos in which *Vegfa* was conditionally deleted in MNs with $Olig2^{MN}$*::Cre* and motor axons were traced with ISL^{MN}*::fGFP*. First, we examined vascular patterns in compound mutants and found that while the peripheral vasculature was as disorganized as in $Plxnd1^{-/-}$ embryos, aberrant vascularization of the MC was corrected by homozygous deletion of *Vegfa* (Figures 7J-7O and S7J-S7M′). Therefore, VEGF released by MNs promotes ectopic vessel formation in the MCs when EC attraction is not counterbalanced by Plexin-D1-mediated repulsion. Likewise, the analysis of motor projections revealed that deletion of *Vegfa* resulted in dose-dependent correction of the distinctive axon guidance errors of $Plxnd1^{-/-}$ embryos, characterized by proximal stalling of epaxial nerves (Figures 7P-7U). These mouse genetic studies indicate that loss of *Plxnd1* offsets the balance of attractive and repulsive signals between MNs and ECs, which can be partially recovered by lowering VEGF-driven attraction toward MNs (Figure 7V).

DISCUSSION

In his first descriptions of growth cones navigating in the embryonic nervous system, Ramón y Cajal captured two main problems of pathfinding: one is the “exquisite chemical sensitivity” that enables axons to select the correct trajectory; the other is their ability to “remove or overcome the obstacles” found along the path (Ramón y Cajal, 1909). Much of the molecular work in the field has focused on how axons respond to guidance cues, whereas the way they confront impediments is not well understood. We show that in order to avoid interference from heterotypic cellular encounters, neurons remodel the tissue microenvironment along their axonal routes by deploying classic guidance factors in a reversal of the typical ligand-receptor signaling orientation. We found MNs release Sema3C to displace ECs from their course. This aversive relationship was unexpected since the interactions between neurons and ECs are typically viewed through the principle of congruency achieved via mutual attraction (Andreone et al., 2015). Nevertheless, the synchronous development of nerves and vessels, together with their reciprocal affinity aimed at metabolic coupling, carry the risk of detrimental contacts that might perturb neural circuit wiring as well as vasculature patterning. The coexistence of angiogenesis and axonal outgrowth is also common in disease and injuries where vessels form close to nerve sprouts to promote repair but might obstruct regrowth due to their chaotic topography at the lesion site (Cattin et al., 2015; Dray et al., 2009; Muramatsu et al., 2012). It is possible that

embryonic mechanisms exploited by axons to bypass vascular obstacles are reactivated during neovascularization of adult tissues.

Axon-endothelial push-pull prevents disruptive contacts and enables congruency

Motor axons avert inappropriate contacts with ECs by counter-balancing attraction mediated by VEGF with repulsion elicited via Sema3C. Neurovascular interactions appear to be mediated by a hierarchical, weighted signaling system that integrates opposing cues from both compartments in order to attain proximity yet preventing interference (Figure 7V). Sema3C/Plexin-D1 and VEGF (presumably via VEGFR2 receptor) constitute primary axes that act in concert with other neuronal/vascular pathways predicted by computational tools. Loss of Plexin-D1 does not affect EC attraction but unmasks vascular signals that obstruct axon projection. Conversely, when attraction is reduced (e.g., by VEGF inactivation), secondary, Plexin-D1-independent, repulsive factors from MNs restore to some extent axon-endothelial crosstalk. It is possible that these responses involve mechanical cues associated with nerves and vessels, which may become dominant when the balance of chemical signals is disrupted. Of note, the mechanosensing property of Plexin-D1, which is independent of Semaphorins, might provide an alternative means to control contacts with axons (Mehta et al., 2020).

EC repulsion prevails at the epaxial turning point while attraction outweighs past this region resulting in nerve-vessel alignment (Figure 7V). These choregraphed interactions might be influenced by the range of action of neurovascular cues. Our assays indicate that Sema3C-repulsion functions at short range, while VEGF-attraction operates at distance. Consistent with its limited diffusion, Sema3C elicits autocrine signaling in MNs (Sanyas et al., 2012). Despite all MNs express Sema3C, nerve-targeting defects in *Plxnd1* and *Sema3C* mutants are restricted to epaxial MNs. The susceptibility of MMC axons might depend on the timing of pathfinding, which coincides with vascular patterning at the epaxial choice point. Other MN subtypes extend in advance of the developing vessels, whereas MMC axons undergo a “waiting period” and this delay may require that they have mechanisms to displace ECs occupying their late-forming trajectory (Figure 7V; Tosney and Landmesser, 1985b). Strong signaling crosstalk was predicted *in silico* between MMC and ECs. Hence, the molecular features of neurons and vessels, together with the spatiotemporal dynamics of their encounters, may dictate specificity and outcomes of neurovascular interactions. Axon-endothelial collisions in *Plxnd1* mutants reverberate in secondary transcriptional changes within MNs. Interestingly, *Sema3C* and *Vegfa* were increased, suggesting that the signaling system controlling neurovascular communication might be under feedback regulation.

Sema3C/Plexin-D1 controls axon-endothelial interactions and spinal cord vascularization

The effects of Sema3C on ECs have been studied in heart development, where Sema3C drives endothelial-to-mesenchymal transition (Plein et al., 2015). On the other hand, recombinant Sema3C countered pathological neovascularization in retinopathy (Yang et al., 2015) and inhibited tumor angiogenesis (Mumblat et al., 2015). Here, we demonstrate a requirement for Sema3C in physiological angiogenesis during CNS vascularization as well as in neurovascular interactions critical for nerve projection. Both motor axon targeting and SC vascularization rely on detection of opposing neuronal signals by ECs. Although

mechanistically related, these appear to be separate processes as underscored by the fact that the axonal phenotypes of *Sema3C* and *Plxnd1* mutants were restricted to epaxial nerves while vessels grew abnormally throughout all MN divisions. Since the onset of vessel ingression in the SC coincides with clustering of MNs and axon outgrowth, it has been proposed that MC vascularization is delayed in order to avoid interference with these processes (Himmels et al., 2017; James et al., 2009). One way, MNs prevent early vascular invasion is through expression of the decoy receptor sFlt1, which limits VEGF availability thereby countering EC attraction (Himmels et al., 2017). We found that *sFlt1* levels were unchanged in the MC of *Sema3C*$^{-/-}$ embryos (data not shown) suggesting that VEGF-titration and Sema3C/Plexin-D1 function independently in a two-tiered system that defines timing and patterning of MC vascularization.

Targeted removal of cellular obstacles in directional migration

All forms of directional cell migration face the challenge of sensing and overcoming impediments. It has remained unclear whether specialized avoidance mechanisms are used to resolve encounters with obstacles during chemotaxis (Grima, 2007). Immune and cancer cells, similar to neuronal growth cones, exert protrusive forces and release proteases to facilitate locomotion in restrictive environments (Gaertner et al., 2022; Murphy and Courtneidge, 2011). However, these seemingly generic solutions might be inadequate alone to account for complex morphogenetic processes that rely on highly orchestrated multicellular interactions during organogenesis and tissue repair. It is therefore likely that obstacle-removal strategies based on selective targeting of signaling crosstalk with subsets of neighboring cells represent common mechanisms to ensure chemotactic movement in different biological contexts beyond nervous system wiring.

STAR METHODS

RESOURCE AVAILABILITY

Lead contact—Further information and requests for resources and reagents should be directed to and will be fulfilled by the lead contact, Dario Bonanomi (bonanomi.dario@hsr.it).

Materials availability—Plasmids, cell lines and mice generated in this study are available from the lead contact upon request pending MTA approval.

Data and code availability

- All original RNA-seq data have been deposited in the Gene Expression Omnibus (GEO) and are publicly available as of the date of publication. The accession number is listed in the key resources table.
- All original code is available from the lead contact upon request.
- Any additional information required to reanalyze the data reported in this work paper is available from the lead contact upon request.

EXPERIMENTAL MODEL AND SUBJECT DETAILS

Mouse lines—*Olig2::Cre* (Dessaud et al., 2007); *Tek*^{EC}*::Cre* (Jax stock# 008863 (Kisanuki et al., 2001); *ISL*^{MN}*::fGFP* (Jax stock# 017952 (Lewcock et al., 2007); *Hb9*^{MN}*::GFP* (Lee et al., 2004); *MN*$^{(218\text{-}2)}$*::GFP* (Amin et al., 2015); *Kdr*^{EC}*::Cherry* (Jax stock# 018542) (Larina et al., 2009); *PlexinD1*^{flox} (Jax stock# 018319) (Zhang et al., 2009); *Plxnd1*-null allele was generated from crossing *PlexinD1*^{flox} with ubiquitous *EIIa-cre* (Jax stock# 003724) (Lakso et al., 1996). *R26-DTA*^{LSL} (Jax stock# 010527) (Wu et al., 2006); *Sema3C*$^{-/-}$ (Feiner et al., 2001); *Sema3E*$^{-/-}$ (Gu et al., 2005); *VEGF*^{flox} (Gerber et al., 1999). *Sema4A*$^{-/-}$ mice were generated with CRISPR/Cas9-mediated gene ablation using 2 guide RNAs (gRNA) targeting the *Sema4A* locus: gRNA#1 (5'-TGGGGTGAGTAGCGGGCATAAGG) targeted intron 1-2; gRNA#2 (5'-GCAGCGTGTCAAAGTCTCGGAGG) targeted exon 3. The two gRNAs were transcribed in vitro with T7 Quick High Yield RNA Synthesis Kit (New England Biolabs Cat# E2050S) and mixed at 15ng/μl each with 30ng/μl of in vitro transcribed, capped and polyadenylated Cas9 mRNA (mMESSAGE mMACHINE T7 Transcription Kit, Thermo Fisher Scientific Cat# AM1344) in microinjection buffer (10 mM Tris-HCl pH 7.4, 0.2 mM EDTA). The freshy prepared mixture was injected into the cytoplasm and pronucleus of CB6F1 zygotes (~2-3pl per embryo), which were reimplanted into CD1 recipient females. Founders were screened by PCR genotyping and confirmed by direct Sanger sequencing. The selected founder carried a ~2-kb genomic deletion encompassing exon 2, which contains the start codon, and part of exon 3. Hemizygous founders were bred for >4 generations with *ISL*^{MN}*::fGFP* mice in CB6F1 back-ground. *Plxnd1*-null, *Sema3*-null, *Sema3E*-null, *VEGF*^{flox} alleles were maintained in C57/BL6N strain. Sema3C mutants were also analyzed in CD1 strain. In some experiments *Plxnd1* mutants were in CB6F1 strain. Phenotype expressivity was similar in different background strains. Embryos were generated by timed mating, and the day on of vaginal plug was designated as embryonic day 0.5 (E0.5). Data were collected from E10-E12.5 embryos of both sexes. There was no evidence of sex-related differences in the reported phenotypes. Mice were maintained in pathogen-free facilities under standard housing conditions with continuous access to food and water. All experimental procedures and handling of animals were approved by the Animal Research Committee of IRCCS San Raffaele Hospital and Salk Institute, and performed in compliance with IACUC guidelines.

Cell lines—Human umbilical vascular ECs (HUVEC; Lonza Cat# C2519A) were cultured in EC Growth Basal Medium-2 (EBM-2; Lonza Cat# CC-3156) supplemented with EGM-2 Endothelial factors (Lonza Cat#CC-4176). Cells were discarded after passage 5. Immortalized cell lines were maintained in DMEM supplemented with 10% FBS, 1% L-Glutamine, 1% Penicillin/Streptomycin (Gibco). AD293 cells are a derivative of the HEK293 cell line (Stratagene Cat# 240085). COS-7 (Cat# CRL-1651) and NIH-3T3 (Cat# CRL-1658) were from the American Type Culture Collection (ATCC). Mouse embryonic fibroblasts (MEF) isolated from E13.5 Swiss Webster mice (Conner, 2001) were cultured in IMDM (Gibco) supplemented with 15% FBS (Euroclone Cat# ECS0180L), 1% L-Glutamine and 1% Penicillin/Streptomycin (Gibco). Cell cultures were maintained at 37°C with 5% CO2. HEK293 (AD293) lines stably expressing Plexin-D1 were generated by clonal selection with 1 μg/ml puromycin after Lipofectamine-based transfection of

Plexin-D1-FLAG-P2A-Puro construct expressing C-terminal FLAG-tagged mouse Plexin-D1 and puromycin-resistance gene under the control of CMV promoter. To generate lines co-expressing Plexin-D1 and either NRP1 or NRP2, HEK-Plxnd1 stable clones were transfected using Lipofectamine 2000 with hyperactive piggyBac transposase [pCMV-HAhyPBase] (Yusa et al., 2011) and Piggy Bac donor plasmids expressing either C-terminal HA-tagged rat Nrp1 or Nrp2 under CAG promoter. Transfected cells were enriched through two rounds of FACS sorting after extracellular staining with 5μg of anti-NRP1 (R&D Systems Cat# AF566) and anti-NRP2 (R&D Systems Cat# AF2215) followed by Alexa647-conjugated secondary antibody.

Primary neuronal cultures—Mouse MN explants comprising LMC and MMC were prepared from the lumbar spinal cord of E12.5 embryos. Chick MN explants were prepared from the motor columns of embryos at Hamburger Hamilton (HH) stage 22-23. Explants were plated on 12mm Poly-D-Lysine (PDL)-treated coverslips (Corning Cat #354086) coated with 50μg/ml laminin (Gibco Cat# 23017015) and cultured in 4-well dishes (Nunc Cat#144444) with MN (MN) media: Neurobasal media containing B27 supplement (Gibco), 2mM L-Glutamine (Euroclone), 1% Penicillin/Streptomycin (Euroclone), 50μM Glutamic Acid (MilliporeSigma), 10ng/ml GDNF (R&D Systems Cat#212-GD). Mouse dorsal spinal cord explants were dissected from the dorsal-most region of the spinal cord of E12.5 embryos and cultured for ~20 hrs in MN media in which GDNF was replaced with 50ng/ml BDNF (Peprotech Cat#450-02).

METHOD DETAILS

ENU screen and mapping of *Drake* mutant—The design of the ENU-mutagenesis screen was previously described (Lewcock et al., 2007). Briefly, fifty DBA/2J mouse males (Jackson Labs) were given intraperitoneal injections of 100 mg/kg ENU (Sigma-Aldrich) once a week for 3 consecutive weeks starting at 8 weeks of age. Eight to ten weeks after injection, animals were mated to ISL^{MN}*::fGFP* mice (maintained on CB6F1/J background, an F1 hybrid between BALB/cJ and C57BL/6J strains). Eighty-eight GFP^{+} F1 males were generated and used in the screen. Six to eight G3 litters derived from each F1 male were examined. Embryos at E12.5 were fixed for 2 hrs in 4% paraformaldehyde (PFA) in PBS, washed in PBS ON, then eviscerated and cleared by consecutive 2-4 hr-incubations (4°C) in 30%, 50%, 80% glycerol (in PBS) on an orbital shaker and flat-mounted between coverslips for GFP visualization under a fluorescence stereomicroscope. After >5 generations of backcrosses, the genomic region containing the *Drake* allele was restricted to a ~10Mb segment on chromosome 6 between dbSNP rs30015050 (108.8Mbp) and rs29870917 (118.5 Mbp) that contains ~200 genes. Total RNA was extracted with RNeasy Plus Mini kit (Qiagen Cat#74134) from the thoracic/brachial spinal cord region and surrounding mesenchymal tissue of three E12.5 mutant embryos, two control (i.e., unaffected) littermates, and one stage-matched DBA/2J embryo. Individual libraries for mRNA sequencing were prepared using Illumina mRNA-Seq Sample Prep Kit (Cat# RS-100-0801). Genome Analyzer IIx platform (Illumina) was used to perform 2x36 cycles of single-end sequencing. Reads were aligned to the reference genome with MOSAIK software to detect SNPs. RNA-seq did not reveal transcriptional and splicing changes in *Drake* mutants. To identify the ENU-asso-ciated base-change, SNPs detected on

chromosome 6 in *Drake* mutants were filtered to remove (1) reference dbSNPs, (2) SNPs found in CB6F1/J control samples, (3) SNPs found in DBA/2J strain. The A>T transversion at 115,994,460 bp (GRCm38/mm10 assembly) of chromosome 6, in the first exon of *Plxnd1* gene, was found in all reads aligned at that location in *Drake* embryos but never in controls or in the parental mouse strains. The resulting C116S mutation in Plexin-D1 is predicted as "deleterious" by PROVEAN software (score: −3.78; cutoff for neutral variants: −2.5).

DNA constructs—To generate CMV-PlexinD1-FLAG construct, a C-terminal FLAG-tag was fused to mouse *Plxnd1* (GenBank: XR_868877.1) using ClonExpress II One Step Cloning Kit (Vazyme Cat# C112-01). After removal of the stop codon, a P2A-Puro cassette was inserted in frame downstream of FLAG-tag to obtain PlexinD-FLAG-P2A-Puro construct. For CMV-PlexinD1-C116S-FLAG, the C116S mutation was introduced with GENEART Site-Directed Mutagenesis System (Thermo Fisher Scientific Cat# A13282) with primers forward 5'-GCAGGCCTCGAGCGAGCAC and reverse 5'-GTGCTCGCTCGAGGCCTGC. Rat Nrp1 (GenBank: NM_145098.2) and rat Nrp2 (GenBank: NM_030869.4) fused to C-terminal HA-tag were cloned in a Piggy Bac donor plasmid under CAG promoter (Ballabio et al., 2020).

Neuronal explant-endothelial cell co-cultures—MN explants or dorsal spinal cord explants dissected from E12.5 mouse embryos were cultured as described above. After 5-6 hrs, 180,000 HUVECs detached with Accutase (Thermo Fisher Scientific Cat# A1110501) were added to the well containing explants. Co-cultures were fixed after ~15 hrs and processed for immunostaining. Co-cultures with other cell lines conformed to this experimental design except that cells were detached with Trypsin 0.25% (Gibco) and 100,000-150,000 MEF, NIH-3T3 or AD293 cells were added to the explants. For live imaging, motor explants were plated on coverslip-bottom 35mm dishes (Corning Cat# 354077) treated as described above and 50,000 HUVECs were seeded directly onto the coverslip after ~6 hrs. Co-cultures were monitored for 13-16 hrs with phase-contrast imaging on an inverted Zeiss Axiovert S100 TV2 microscope equipped with temperature/CO2/humidity-controlled environmental chamber (OkoLab) and autofocus module, and were fixed/stained at the end of the imaging session. For chick MN explants, pN1-EGFP construct (Clontech) was electroporated "in-ovo" in the neural tube of HH 17-18 embryos using a square wave electroporator (BTX) and eggs were incubated in a humidified and temperature-controlled chamber (37,5°C; humidity 55%). Explants were prepared at HH 22-23. When indicated, neutralizing anti-Plexin-D1 antibody (5μg/ml) (R&D Systems Cat# AF4160) was added to the co-cultures at the time of HUVEC seeding. Neutralizing anti-VEGF164 antibody (2.5μg/ml) (R&D Systems Cat# AF564) was added to motor explants 1 hr prior to HUVEC seeding. Both antibodies were maintained for the duration of the experiment. For "low-laminin" condition, PDL-treated coverslips were coated with 5 μg/ml laminin. For axon growth assays with HUVEC-conditioned media, HUVECs were cultured for 24 hrs in serum-free EBM-2 media with half concentration of factors. The media was collected, passed through 0.22μm filters and concentrated with 3kDa Amicon Ultra Centrifugal Filter Units (SigmaMillipore Cat# UFC900324). Motor explants were then cultured for 24 hrs in MN media supplemented with a volume of concentrated media

estimated to be conditioned by the same number of HUVECs used in co-cultures (180,000 cells).

RNA interference in HUVEC—HUVECs at 60-70% confluency were transfected in 6-well plate with 5μM control siRNA (Non-targeting Pool; Dharmacon Cat#D-001810-10-05), 5μM *Plxnd1* siRNA (Human PLXND1 (23129) siRNA– SMARTpool; Dharmacon Cat# L-014121-01-0005), 10μM *Nrp1* siRNAs (Human NRP1 (8829) siRNA–SMARTpool; Dharmacon Cat# L-019484-00-0005) or 10μM *Nrp2* siRNAs (Human NRP2 (8828) siRNA–SMARTpool; Dharmacon Cat#L-017721-00-0005) using 4μl of DharmaFECT4 transfection reagent (Dharmacon Cat# T-2004-01) in 400μl of Opti-MEM (Gibco Cat# 31985070) after 20 min incubation at RT. Cells were incubated ON with the transfection mixture and used 48 hrs later for co-cultures and other in vitro assays. Knockdown efficiency was tested routinely by quantitative RT-PCR and western blotting.

Collapse assay in COS-7 cells—COS-7 cells transfected in 6-well plate with 6μl of Lipofectamine 2000 and 2μg of plasmid expressing C-terminal FLAG-tagged Plexin-D1 (WT or C116 mutant), were transferred to PDL-coated coverslips and treated at 48 hrs after transfection with 7nM AP-Sema3E for 1 hr in Opti-MEM. After fixation with 4%PFA/4% sucrose for 30 min, cells were stained with anti-FLAG antibody and Alexa488-conjugated Phalloidin. Cells were classified as “collapsed” based on a ~70% average reduction in surface area and the presence of actin-rich protrusions.

Cell-cell repulsion assay—For HUVEC-HEK repulsion assays, HUVECs were transfected with the indicated siRNAs as described above and after 24 hrs 70,000 cells were transferred to 12mm PDL-coated coverslips. On the same day, AD293 were transfected in 24-well plate with pN1-EGFP (0.09μg) (Clontech) and either AP-Fc, or AP-Sema3E or AP-Sema3C (0,35μg) using with 1.3μl Lipofectamine 2000 [1:3 DNA:Lipofectamine ratio]. After 24 hrs, 2,000 transfected AD293 were seeded on top HUVEC monolayer. For HEK:Sema/HEK-Receptor assays, 2,000 AD293 cells co-transfected with GFP and AP-Sema constructs were seeded on a monolayer of naïve AD293 or cell lines stably expressing receptors genes. Co-cultures were fixed 16 hrs later and stained for GFP and F-actin (with Alexa555-conjugated Phalloidin). To quantify cell repulsion, the cell-free region around randomly selected GFP^+ HEKs was manually traced using the freehand tool of ImageJ software, and the pixel area was normalized by the number of GFP^+ HEKs at each site.

Scratch wound healing and cell proliferation assays—For scratch would healing assay, HUVECs transfected for 48 hrs with control or *Plxnd1*-targeting siRNAs were seeded in 96-well plate at 50,000 cells/well in complete EBM-2 media. After 24 hrs, the cell monolayer was scratched with a 96-pin Wound Maker (IncuCyte, Essen Bioscience). Cells were washed twice with PBS and incubated for 18 hrs in complete MN media with or without recombinant Sema3C-Fc (500 ng/ml; R&D Systems Cat# 5570-S3). The wound area was imaged every 15 min using the IncuCyte Zoom system and the rate of gap closure was quantified automatically with IncuCyte Analysis Software by measuring the relative wound confluence at each time point. For cell proliferation assay, 30,000-40,000 control or *Plxnd1* knockdown HUVECs were seeded in 24-well plate containing either complete

EBM-2 media or MN media, let recover for 1 hr and imaged with IncuCyte system for 36 hrs to automatically measure cell growth rates based on normalized confluence area.

Transwell migration assays—Approximately 30-40 motor explants were plated on coverslips in a 24-well plate as described above and cultured for 48 hrs to precondition MN media (600 μl). The lower side of Transwell inserts (8μm pore size; Corning Cat# CLS3422) was coated with 10 μg/ml fibronectin (Corning Cat# 354008) for 90 min and blocked with 0.2% BSA/PBS until the inserts were placed in the wells containing explants (or control wells with basal MN media). HUVECs (~75,000 cells) resuspended in plain EBM-2 containing 0.2% BSA were seeded in the upper chamber of the inserts and allowed to migrate for 6 hrs. For VEGF neutralization experiments, 2.5 μg/ml of anti-VEGF antibody (R&D Systems Cat# AF564) or control goat IgG (Jackson ImmunoResearch Cat# 005-000-003) were added to the explants 2 hrs before HUVEC plating and left in the lower chamber for the duration of the experiment. To study HUVEC migration in response to recombinant factors, the inserts were placed in wells containing plain EBM-2 (control) or EMB-2 supplemented with 100ng/ml human VEGF165 (Miltenyi Biotec Cat# 130-109-395) or 500ng/ml mouse SDF-1a/Cxcl12 (Prospec Cat# CHM-324). At the end of the experiment, cells that remained in the upper side of the insert membrane were mechanically removed with a cotton swab, while those migrated to the lower side were fixed with 4% PFA, stained with crystal violet and imaged with a Zeiss Axio Zoom.V16 stereo microscope.

AP-fusion protein binding assays—AP-fusion proteins were prepared from AD293 cells transfected with the indicated constructs (10μg in 10cm dish) using Lipofectamine 2000 (3μl Lipofectamine:1μg DNA). After transfection, cells were cultured in 5ml Opti-MEM and the media was collected and replaced for 3 consecutive days, passed through a 0.22μm cell strainer and concentrated on 30kDa Amicon Ultra Centrifugal Filter Units (SigmaMillipore Cat# UFC903024). Ligand concentration was determined as previously described (Flanagan and Leder, 1990). Cell binding assays were performed according to previous protocols (Gitler et al., 2004). COS-7 cells were transfected for 48hrs with the indicated constructs using Lipofectamine, washed with PBS, incubated at RT with AP-Sema3E (5nM for 75 min) or AP-Sema3C (1nM for 90 min), fixed for 15 min with 4% PFA (RT), washed and incubated in PBS at 65°C for 3 hrs to inactivate endogenous alkaline phosphatases. AP-Sema binding was detected by incubating cells at RT for 15-30 min in AP substrate buffer (100mM Tris pH9.5, 100mM NaCl, 50mNMgCl2, 0.1% Tween, 0.33mg/ml NBT and 0.05 mg/ml BCIP). AP signal intensity in individual cells was measured on inverted grayscale images using Fiji/ImageJ software. AP-Sema3E protein binding to tissue sections was performed as described (Feiner et al., 1997).

Western blotting—COS-7 cells transfected for 48 hrs in 6 well-plate with Plexin-D1 WT and C116S constructs (1.7μg) using Lipofectamine 2000 were lysed in 400μl/well SDS-lysis buffer (150mM NaCl, 50mM TrisHCl pH7.4, 10mM EDTA, 1% Tx-100, 0.1% SDS) supplemented with protease (Merck/Roche Cat# 4693132001) and phosphatase (Thermo Fisher Scientific Cat# 78420) inhibitor cocktails, cleared by centrifugation at 13,000 xg for 15 min (4°C) and resuspended in NuPAGE LDS Sample Buffer (Thermo Fisher Scientific Cat# NP0007). To detect Plexin-D1 in *Drake* mutants, the thoracic-brachial spinal

cord segment and surrounding tissue from individual E12.5 embryos were homogenized in 200µl SDS-lysis buffer with protease/phosphatase inhibitors, cleared by centrifugation and resuspended in NuPAGE LDS Sample Buffer. The whole spinal cord, or isolated dorsal and ventral regions, from E12.5 embryos were lysed in 80-100 µl of modified RIPA buffer (150mM NaCl, 50mM TrisHCl pH7.4, 10mM EDTA, 1% NP40, 0.5% Sodium Deoxycholate) with protease/phosphatase inhibitors, cleared by centrifugation and resuspended in Laemmli Sample Buffer (Biorad Cat# #1610747). The same lysis buffer (80-100 µl/well) and procedures were used to prepare total protein extracts from siRNA-treated HUVECs and MN explants cultured for 48hrs on 12mm coverslips as described above. Protein samples were quantified with Bradford protein assay (Bio-Rad Cat #5000006), run on handcast 8-10% SDS-PAGE gels or NuPAGE 4-12% Bis-Tris gels (Thermo Fisher Scientific), transferred on nitrocellulose membranes (Amersham/ Merck Cat# GE10600002) and probed with the indicated antibodies. Antibodies used for immunoblotting were: goat anti-PlexinD1 (1:500-1:800, R&D systems Cat# AF4160), rabbit anti-GAPDH (1:10,000, Cell Signaling Cat# 2118), rabbit anti pan-Actin (1:1000; Cell Signaling Cat# 4968), rat anti-Semaphorin3C (1:500; R&D Systems Cat# MAB1728).

Quantitative RT-PCR—RNA was extracted from the dorsal and ventral spinal cord of E12.5 embryos with RNeasy Mini Kit (Qiagen). cDNA was synthesized from 500ng RNA with M-MLV reverse transcriptase (Thermo Fisher Scientific Cat# 28025013) and random primers (Thermo Fisher Scientific Cat# N8080127), diluted to 40µl in molecular biology-grade water and used for real-time quantitative PCR with SYBR Select Master Mix (Thermo Fisher Scientific Cat#4472913). Real-time PCR reactions were performed in triplicate. Target mRNA levels were normalized to the *GAPDH* mRNA levels from the same RT reactions. Primer sequences are reported in Table S6.

Immunofluorescence, immunohistochemistry and in situ hybridization— Explants and cells were fixed with 4%PFA/4% sucrose in PBS for 30 min (RT), incubated for 2 hrs (RT) with primary antibodies diluted in 1% BSA/0.1% Tx-100 in PBS and, after 3 washes in PBS, with fluorophore-conjugated secondary antibodies in the same buffer for 1 hr (RT). Samples were washed in PBS, stained with DAPI and mounted with ProLong Diamond Antifade Mountant (Thermo Fisher Scientific Cat#P36965) or PermaFluor Mounting Medium (Thermo Fisher Scientific Cat# TA-030-FM).

For cryosectioning, embryos were fixed in 4% paraformaldehyde diluted in PBS for 2-3 hrs (4°C), washed extensively in PBS, cry-oprotected in 30% sucrose for 2-4 hrs at 4° C, and embedded in OCT compound (Sakura Cat# 4583). Cryosections (20-40µm) were incubated with primary (ON, 4°C) and secondary antibodies (2-3 hrs, RT) in PBS containing 1% BSA/0.2% Tx-100. Samples were washed in PBS, stained with DAPI and mounted with PermaFluor Mounting Medium or Fluorescent Mounting Medium (Dako Cat# Code S3023).

Immunohistochemistry for Plexin-D1 was carried out on 20µm sections. After washes in PBS, sections were dehydrated in an ascending series of methanol (MeOH 25% in PBS; MeOH 50% in PBS; MeOH 75% in H2O; MeOH 100%), incubated in 3% H_2O_2 in MeOH for 15 minutes at RT to block endogenous peroxidases, and rehydrated in a descending methanol series. Sections were incubated in blocking solution (1 mg/mL BSA; 10% FBS;

0.1% TritonX-100 in PBS) for 1h at RT, and then with primary goat anti-PlexinD1 diluted 1:200 in the same buffer ON at 4°C. After 3 washes in PBS, sections were incubated with secondary biotinylated rabbit anti-goat IgG (Vector lab Cat# PK-6105) diluted 1:200 in blocking solution for 90 min at RT. Immunoreactive signal was amplified with ABC working solution (Vector lab Cat# PK-6105) for 90min at RT. Chromogenic detection was performed with DAB peroxidase substrate (Vector lab Cat# SK-4100). Slides were mounted with Glycergel medium (Dako Cat# C0563).

Primary antibodies used for immunostaining were: chicken anti-GFP (1:500; Abcam Cat# ab13970), rabbit anti-GFP (1:1000; Thermo Fisher Scientific Cat# A6455), mouse anti-GFP (1:1000; Thermo Fisher Scientific Cat# A11120), mouse anti-FLAG (1:1000; Sigma-Aldrich Cat# F1804), goat anti-Plexin-D1 (1:200-1:500; R&D Systems Cat# AF4160), goat anti-VE-Cadherin (1:300; R&D Systems Cat# AF938), rabbit anti-VE-Cadherin (1:1000; Abcam Cat# ab33168), mouse anti-βIII Tubulin (1:1000; Abcam Cat#ab7751), rabbit anti-Fsp1 (1:250; Millipore Cat# 07-2274), rat anti-CD31 (1:1000; BD Biosciences Cat# 550274); goat anti-CD31 (1:1000; R&D systems Cat# AF3628); rabbit anti-VAChT (1:1000; Synaptic Systems Cat# 139103); rabbit anti-Isl1/2 1:2,500 (Ericson et al., 1992); rabbit anti-Hb9 #6055 1:8,000 (Thaler et al., 1999). Secondary antibodies were: goat or donkey anti-rabbit/mouse/goat/rat Alexa Fluor 488-, 555-, 647-conjugated (1:1000; Thermo Fisher Scientific). Alexa Fluor 488 Phalloidin (1:100; Thermo Fisher Scientific Cat# A12379) and Alexa Fluor 555 Phalloidin (1:100; Thermo Fisher Scientific Cat# A34055) were added with the secondary antibody mix.

In situ hybridization was carried out on 20 μm cryostat sections following standard procedures with digoxigenin-labeled RNA anti-sense probes: mouse *Plxnd1* (GenBank: NM_026376; 3544-6913bp) (Gu et al., 2005); mouse *Vegfa* (GenBank: NM_001317041.1; 1431-1849bp) (Ruiz de Almodovar et al., 2011); mouse *Sema3C* (GenBank: NM_013657.5; 546-1441bp) cloned in pCRII-Topo (Thermo Fisher Scientific); mouse *Sema3E* (GenBank: NM_011348; 1130-1920bp) cloned in pCRII-Topo. RNA scope probe for mouse *Plxnd1* (ACD Bio-Techne Cat# 405931) was used according to the manufacturer's instructions,

Cell surface staining—COS-7 cells were transfected with C-terminal FLAG-tagged Plexin-D1 (WT or C116 mutant) and cultured for 48 hrs on PDL-treated coverslips. Surface-targeted Plexin-D1 was detected by staining live cells with goat anti-Plexin-D1 antibody to the extracellular domain (R&D Systems Cat #AF4160) diluted 1:200 in 3% BSA/DMEM at 11°C for 15 min. Cells were fixed with 4% PFA/4% Sucrose in PBS for 10min (RT), followed by incubation with Alexa555-conjugated anti-goat antibody (1:500; Thermo Fisher Scientific) in 1% BSA/PBS for 1 hr (RT). The total pool of Plexin-D1 was detected by intracellular staining with anti-FLAG antibody (1:1000; MilliporeSigma Cat# F1804) in 1% BSA/PBS containing 0.1% Tx-100 for 1 hr (RT), revealed with Alexa647-conjugated secondary antibody (1:000; Thermo Fisher Scientific) in the same buffer for 1hr (RT).

Embryo whole mount staining and tissue clearing—Whole mount embryo staining with rat anti-CD31 antibody (BD Biosciences) was performed as previously described (Zhang et al., 2009). For staining of thick tissue sections, embryos were fixed in 4% PFA ON at 4°C, dehydrated in an ascending methanol series (50% MeOH in PBS; 80% MeOH

in H2O; 100% MeOH - 90min each at RT on a rocker), bleached with 6% H_2O_2 in MeOH ON at 4°C on a rocker, and rehydrated in a descending methanol series. Embryos were embedded in 5% low-melting agarose (GellyphorLM, Euroclone Cat# EMR911100) in PBS and sectioned with a vibratome at 1mm thickness. Agarose was removed under a dissection microscope and sections were incubated in PBSGT [0.2% gelatin, 0.5% TritonX-100, 0.01% Thimerosal (Sigma/Merck cat# T8784-5G) in PBS] for 24hrs at RT on a rocker. Primary antibodies were diluted in PBSGT with 10 mg/ml saponin and incubated for 7 days at RT on a rocker. Sections were washed 6 times over one day with PBSGT, then incubated with secondary antibodies in PBSGT with 10 mg/mL saponin ON at RT on a rocker. After 6 washes in PBSGT, sections were stored in PBS at 4°C until clearing.

Primary antibodies used for whole mount staining were: rat anti-CD31 (1:500; BD Biosciences); goat anti-CD31 (1:1000; R&D Systems); rabbit anti-GFP (1:5000; Thermo Fisher Scientific). Secondary antibodies (from Thermo Fisher Scientific) were: donkey anti-Rabbit AlexaFluor-488 (1:1000; Cat# A21206); goat anti-Rat AlexaFluor-546 (1:1000; Cat# A11081); donkey anti-goat AlexaFluor-555 (1:1000; Cat# A21432). Sections were cleared after staining with X-CLARITY Tissue Clearing System (Logos Biosystems). Samples were incubated in Hydrogel Solution (Logos Biosystems Cat# C1310X) for 24 hrs at 4°C, transferred in X-CLARITY Polymerization System for 3 hrs at 37°C, then washed several times in Electrophoretic Tissue Clearing Solution (Logos Biosystems Cat# C13001) and incubated ON at RT in the same solution for clarification. Samples were washed extensively in PBS and incubated in X-Clarity Mounting Solution (Logos Biosystems Cat# C13101) 1h at RT before imaging with a Nikon A1 MP multiphoton microscope with Coherent Chameleon Ultra II using Apo LWD 25 X (NA 1.1) Water Plan objective. 3D-image stacks were analyzed with Arivis 4D software.

Isolation and RNA-sequencing of motor neurons and endothelial cells—ECs and MNs were simultaneously isolated by FACS from E12.5 *Plxnd1*$^{-/-}$ embryos or control littermates (WT or *Plxnd1*$^{+/-}$) harboring *ISL*^{MN}*::fGFP* and *Kdr*^{EC}*::Cherry* reporters. The spinal cord and surrounding meninges –along with attached DRGs– were dissected, pooled according to genotype, and dissociated with Papain Dissociation System (Worthington Biochemical Cat# LK003153). After 15 min rotation at 37°C, tissues were mechanically triturated, centrifuged at 300 xg for 5 min and the reaction was blocked with DNase/albumin-inhibitor solution. Dissociated cells were pelleted, resuspended in Neurobasal media without phenol red (Gibco Cat# 12348017) supplemented with 2% Horse Serum/1% L-Glutamine, and passed through a 35mm cell strainer (BD Falcon Cat# 08-771-23). GFP$^+$ MNs and Cherry$^+$ ECs were purified on a BD Influx Cell Sorter and collected directly into RLT lysis buffer (Qiagen) containing β-mercaptoethanol. RNA was isolated with RNeasy Mini Kit and on-column DNase digestion (Qiagen RNase-Free DNase Set Cat# 79254). Each sample contained 100,000-300,000 GFP$^+$ MNs or mCherry$^+$ ECs collected from 2 control and 2 mutant embryos in each of 3 independent experiments. A total of 6 EC samples (3 control, 3 *Plxnd*$^{-/-}$) and 6 MN samples (3 control, 3 *Plxnd*$^{-/-}$) were quantified with Agilent 2100 Bioanalyzer prior to preparation of mRNA-sequencing libraries (50bp or 75bp single-end) with Illumina TruSeq RNA Library Preparation Kit (v2). Libraries were sequenced with Illumina NextSeq500 or HiSeq 2500 platform.

For RNA-seq of spinal and meningeal ECs, the ventral region of the spinal cord and meninges were dissected from E12.5 *Kdr^{EC}::Cherry* wild-type embryos, pooled separately and dissociated as described above. ECs (mCherry^{+}) were isolated on BD Influx Cell Sorter and collected in Trizol LS Reagent (Thermo Fisher Scientific Cat# 10296010). Approximately 170,000 meningeal and ~40,000 spinal ECs were collected from an average of 7 embryos in each experiment. Stranded mRNA-sequencing libraries (75 bp single-end) were prepared with Illumina TruSeq RNA Library Preparation Kit (v2) from 5 RNA samples for each tissue. Libraries were sequenced with Illumina NextSeq 500 platform.

Microscopes—Fluorescence-assisted microdissection was performed with Zeiss Lumar V12 and Zeiss Axio ZoomV16 stereo microscopes. The same instruments were used for imaging anti-CD31 and AP-Sema3E staining in embryo whole-mounts. Confocal images were acquired with an Olympus Fluoview FV1000, Olympus Fluoview FV3000RS and Leica TCS SP8 SMD FLIM Laser Scanning Confocal microscopes. Thick cleared tissue sections were imaged with Nikon A1 MP multiphoton microscope with Coherent Chameleon Ultra II. For immunohistochemistry and in situ hybridization, color brightfield images were acquired with Zeiss AxioImager M2m microscope. Cell surface/intracellular staining images were acquired with Zeiss Axio Observer Z1 microscope equipped with Hamamatsu EM 9100 camera.

QUANTIFICATION AND STATISTICAL ANALYSIS

Computational analysis

RNA-sequencing data analysis: After trimming, reads were aligned using STAR aligner (Dobin et al., 2013) on the GRCm38 (mm10) genome and counted with featureCounts (Liao et al., 2014) on Gencode annotation release M22 (Harrow et al., 2012). Raw counts were batch-corrected with ComBat-seq (Zhang et al., 2020) and differential gene expression was assessed in R/BioConductor (Huber et al., 2015) using the DESeq2 package (Love et al., 2014). Gene ontology and pathway discovery were performed with Enrichr (Xie et al., 2021) and GeneCodis3 (Tabas-Madrid et al., 2012) gene enrichment tools. The accession number for the RNA-sequencing data reported in this paper is GEO: GSE207942.

Single-cell RNA-sequencing data of *Hb9^{MN}::GFP^{+}* spinal MNs isolated from E12.5 embryos (Amin et al., 2021) (samples WT1 and WT2 at accession ArrayExpress: E-MTAB-10571) were aligned and counted as described above. UMI and barcodes were identified using UMI-tools (Smith et al., 2017). WT1 and WT2 datasets were analyzed independently and then integrated, following the Seurat V4 standard pipeline (Hao et al., 2021). Clusters were identified by a shared nearest neighbor (SNN) modularity optimization-based clustering algorithm at the resolution of 0.4. Single-cell RNA sequencing data from ECs isolated from limb of embryos at E11.0, E12.0 and E13.0 were analyzed by sub-setting the global count matrix downloaded from https://mouse-limb.cells.ucsc.edu/ (He et al., 2020). Gene counts were analyzed with the Seurat V4 standard pipeline. Gene expression in HUVEC was derived from two independent bulk RNA-seq datasets ([Madugundu et al., 2019] GEO: GSM3181634 and [Palikuqi et al., 2020] GEO: GSM3761214-217). Read counts were normalized by library size and gene length to obtain expression values, and averaged between replicates.

Expression Weighted Celltype Enrichment analysis: EWCE package with *Bootstrap.enrichment.test* (10,000 random gene sets) (https://doi.org/10.18129/B9.bioc.EWCE) was used to determine the relative distribution of DEGs (158 upregulated, 41 downregulated; DESeq2 adj. $p < 0.1$) identified by bulk RNA-seq of MNs isolated from *Plxnd1*$^{-/-}$ E12.5 embryos, within MN subtypes defined in the integrated Seurat object (WT1+WT2) from scRNA-seq MN data (Amin et al., 2021).

Cell-cell interaction analysis: After merging of Seurat objects derived from the reanalysis of scRNA-seq datasets of ECs (He et al., 2020) and MNs (Amin et al., 2021), gene counts were mapped to human gene homologs and normalized for the individual cell output. The resulting expression matrix was then analyzed using CellPhoneDB software (github.com/Teichlab/cellphonedb) (Efremova et al., 2020), using the *statistical analysis* method. A curated set of ligand-receptor pairs related to cell guidance and angiogenesis was obtained by filtering the mouse and human CellTalkDB database (http://tcm.zju.edu.cn/celltalkdb/index.php) against gene sets KEGG: hsa04360 (axon guidance), GO:0001525 (angiogenesis), GO:0042056 (chemoattractant activity), GO:0045499 (chemorepellent activity) and removing annotated interactions involving intracellular molecules (GNAI2, HRAS, ITGB1BP1, TLN1), genes not expressed in spinal or meningeal ECs (CD44, TLR4), and cis interactions (APP_DCC, ADAM10_EPHA3, CNTN2_NRP1), yielding a non-redundant list of 675 ligand-receptor pairs (Table S4). An “interaction score” = $\log_{10}$(ligand_expression) + $\log_{10}$(receptor_expression) was calculated between MMC neurons and ECs based on average expression of each gene of the pair in scRNA-seq data. Out of 1350 computed interactions (675 x 2), 134 displaying highest scores (top 10%) were retained for further analysis. Of these pairs, 66 had ligands expressed in MMC and receptors in ECs, while 68 had ligands expressed in ECs and receptors in MMC.

Image analysis and quantification—Images used for quantification were acquired using the same microscope settings and adjusted to the same background levels whenever possible. Images were processed with Fiji/ImageJ, Adobe Photoshop or Arivis 4D software. For quantification of motor axon guidance defects, a “phenotype score” was calculated as the product between the number of ectopic *ISL*^{MN}*::fGFP*$^{+}$ axon bundles and the number of affected motor roots manually counted in flat-mounted embryos under a fluorescence stereomicroscope. Axonal/vascular intensity profiles (Figures 2N and 2O) were measured with the Color Profiler plugin of Fiji/ImageJ software along a 200 px trace spanning the MMC choice point. Vascular density in *Olig2*^{MN}*::Cre*; *DTA*^{LSL} vs. *control* embryos was measured across a 100 x 100 px ventral root area encompassing the motor exit point. CD31^{+} vessels present in this region were thresholded in Fiji/ImageJ software and the total vascular area (px) was measured. The same procedure was used to quantify spinal cord vascularization within the motor columns or dorsal regions manually defined based on marker expression and anatomical location. For MN quantification, the entire motor columns or MMC division were manually traced with “lasso” tool in Adobe Photoshop, based on marker expression (motor column: Hb9^{+}/ISL1/2^{+}; MMC: Hb9^{+}/*ISL*^{MN}*::fGFP*^{high}/Isl1^{high}) and mediolateral position. MN nuclei (Hb9^{+} or ISL^{+}) were thresholded in Fiji/ImageJ and the total px area was measured as a proxy for cell count. A semi-automated quantification of motor explants outgrowth from was performed using the FeatureJ plugin of Fiji/ImageJ

software to measure the total axonal area (#pixels) after removal of the signal associated with the cell bodies (Bonanomi et al., 2012). The extent of HUVEC repulsion in explant co-cultures was quantified by manually tracing and measuring the cell-free area (#px) around individual explants. For quantification of Plexin-D1 surface staining, individual transfected COS-7 cells were thresholded with Fiji/ImageJ and the ratio between mean fluorescence intensity of surface-associated and total signal (derived from intracellular staining) was calculated after subtraction of background fluorescence. For quantification of Transwell assays, tiled images spanning the bottom side of the insert membrane were thresholded with Fiji/ImageJ software to generate a binary mask of migrated cells, which were automatically counted with "analyze particles" function after defining a range size that was maintained for all conditions. Additional quantification approaches are described in the corresponding method section. Statistical analysis was performed with GraphPad Prism V8.4.0 software. Statistical details of the experiments are found in the figure legends.

Sample size for measurements reported in the Figures were:

Figure 1O: N transfected cells scored per condition: ~1000 from 2 independent experiments

Figure 2G: N embryos: Plxnd1$^{C116S/+}$ [Ctrl] (18); Plxnd1$^{C116S/C116S}$ [C116S] (18); Plxnd1$^{-/-}$ (22); Olig2^{MN}::Cre;Plxnd1$^{C116S/fl}$ [Plxnd1$^{MN\Delta}$] (9); Tek^{EC}::Cre; Plxnd1$^{C116S/fl}$ [Plxnd1$^{EC\Delta}$] (17).

Figures 2N and 2O: N ventral roots: *Ctrl* (9; 6 embryos); *Plxnd1*$^{-/-}$ (14; 9 embryos).

Figure 3L: N motor columns: *Control* [*Ctrl*] (60; 19 embryos, heterozygous or *WT* littermates); *Plxnd1*$^{C116S/C116S}$ [*C116S*] (22; 6 embryos); *Plxnd1*$^{-/-}$ (58; 12 embryos).

Figure 3M: N spinal cords: *Ctrl* (34; 23 embryos, heterozygous or *WT* littermates); *Plxnd1*$^{C116S/C116S}$ [*C116S*] (10; 6 embryos); *Plxnd1*$^{-/-}$ (25; 16 embryos).

Figure 4C: N explants: Control (26); *siPlxnd1* (23).

Figure 4J: N explants: Control (73); si*Plxnd1* (50); anti-Plxnd1 (30); low laminin (35); MEF (47); 3T3 (28).

Figure 4K: N explants: Control (43); si*Plxnd1* (23); anti-Plxnd1 (18).

Figure 4L: N explants: no-EC (23); control EC (66); si*Plxnd1* EC (69).

Figure 4M: N explants: control media (25); conditioned media (23).

Figure 5E: N motor columns: *Control* [*Ctrl*] (36; 9 embryos, *Sema3C*$^{+/-}$ or *WT* littermates); *Sema3C*$^{-/-}$ (66; 7 embryos); *Sema3E*$^{-/-}$ (54; 5 embryos); *Sema4A*$^{-/-}$ (52; 5 embryos).

Figure 5J: N embryos: *Sema3C, Sema3E, Sema4A* heterozygous [*Ctrl*] (>30); *Sema3E*$^{-/-}$ (17); *Sema4A*$^{-/-}$ (9); *Sema3C*$^{-/-}$ (41).

Figure 5K: 41 *Sema3C*$^{-/-}$ embryos.

Figure 5M: N independent wells from 3 experiments: Ctrl/untr. (26); Ctrl/Sema3C (21); si*Plxnd1*/untr. (28); si*Plxnd1*/Sema3C (20)

Figure 5P: N explants: WT (74); *Sema3E*$^{+/-}$ (57); *Sema3E*$^{-/-}$ (60); *Sema3C*$^{+/-}$ (42); *Sema3C*$^{+/-}$ (113).

Figure 5Q: N fields of view: >95 from 3 independent experiments.

Figure 5U: N explants: control (37); si*Nrp1* (37); si*Nrp2* (65).

Figure 5Z: N explants: control HEK (29); HEK-*Plxnd1* (34); HEK-*Plxnd1/Nrp1* (55); HEK-*Plxnd1/Nrp2* (40)

Figure 7D: N=Transwells from >3 experiments: basal (13); motor-conditioned media [MN] (11), MN/VEGF^{NAb} (6)

Figure 7E: N=explants: Ctrl/untr. (25); Ctrl/VEGF^{Nab} (39); siPlxnd1/untr. (54); si*Plxnd1*/VEGF^{Nab} (70).

Figure 7N: N motor columns: Control [*Ctrl*] (60; 19 embryos, *Plxnd1* heterozygous or *WT* littermates); *Plxnd1*$^{-/-}$ (58; 12 embryos); *Plxnd1*$^{-/-}$;*VEGF*^{het} (82; 4 embryos); *Plxnd1*$^{-/-}$;*VEGF*^{flox} (61; 6 embryos).

Figure 7T: N embryos: *Plxnd1*$^{-/-}$ (22) [also shown in Figure 2G]; *Plxnd1*$^{-/-}$;*VEGF*^{het} (14); *Plxndr*$^{-/-}$;*VEGF*^{flox} (7)

Figure S1K: N cells: WT (89), C116 (78).

Figure S1L: N=~150 cells from 3 experiments.

Figure S3C: N ventral roots: *Ctrl* (29; 8 embryos); *DTA* (28; 9 embryos).

Figures S3J and S3K: N MCs: *Ctrl* (41; 11 embryos, heterozygous or *WT* littermates); *Plxnd1*$^{C116S/C116S}$ [*C116S*] (14; 4 embryos); *Plxnd1*$^{-/-}$ (29; 7 embryos).

Figure S3R: N MCs: *Control* [*Ctrl*] (34; 8 embryos, heterozygous or *WT* littermates); *Plxnd1*$^{-/-}$ (49; 10 embryos).

Figure S4O: N explants: motor (61); dorsal (39).

Figure S4P: N explants: control EC (40); si*Plxnd1* EC (27).

Figure S4Q: N, 12 wells per condition.

Figure S5H: N embryos: *WT* (3), *Sema3C*$^{+/-}$ (10).

Figure S5I: N explants: *Ctrl* (48), *Sema3C*$^{-/-}$ (42).

Figure S5M: N experiments: si*Plxnd1* (4) si*Nrp1* (6) si*Nrp2* (6).

Figure S5O: N, cells from 3 experiments: Plexin-D1^{WT} (478), NRP1 (836), Plexin-D1^{WT}/NRP1 (959), Plexin-D1^{C116S}/NRP1 (1026).

Figure S5R: N=20-35 fields of view.

Figure S7C: N=Transwells from 3 experiments: basal media (4); Cxcl12 (9) Cxcl12/VEGF^{NAb} (7).

Figure S7H: N=Transwells from >2 experiments: Ctrl/basal (5); Ctrl/MN (4); si*Plxnd1*/basal (5); si*Plxnd1*/MN (4).

Figure S7I: N= 4 Transwells per group from 2 experiments.

Supplementary Material

Refer to Web version on PubMed Central for supplementary material.

ACKNOWLEDGMENTS

We thank Joe Lewcock for the design of the mouse screen; Karen Lettieri and Miriam Gullo for technical assistance; Shawn Driscoll for bioinformatic analysis; Jonathan Raper and Sophie Chauvet for Sema3C KO mice; Christiana Ruhrberg and Genentech, Inc. for *Vegfa-flox* mice; Chenghua Gu for AP-Sema3C and *Plxnd1* riboprobe plasmids; Carmen Ruiz de Almodóvar and Peter Carmeliet for *Vegfa* riboprobe; Roman Giger for Nrp1-HA and Nrp2-HA plasmids; Akiyoshi Uemura for mouse *Plexin-D1* clone; Luca Tiberi for PiggyBac system plasmids; Andrea Ditadi for MEFs; Nasun Hah and the Next-Generation Sequencing Core of Salk Institute; Yelena Dayn and the Transgenic Core Facility of Salk Institute; and the advanced microscopy laboratory (ALEMBIC) of San Raffaele Hospital for instrumentation and expertise. L.F.M. was supported by fellowship PD/BD/114170/2016 from the Foundation for Science and Technology Portugal. S.d.P. was supported by AIRC/CRUK/ AECC Accelerator Award (ECRIN-M3) A29370. Funding sources: European Research Council Starting Grant 335590 and Giovanni Armenise-Harvard Foundation Career Development Award to D.B.; Howard Hughes Medical Institute Investigator Grant, National Institute of Neurological Disorders and Stroke (NINDS) RO1 NS123160-01, the Sol Goldman Charitable Trust, and Benjamin H. Lewis Chair in Neuroscience to S.L.P.

INCLUSION AND DIVERSITY

We support inclusive, diverse, and equitable conduct of research.

REFERENCES

Amin ND, Bai G, Klug JR, Bonanomi D, Pankratz MT, Gifford WD, Hinckley CA, Sternfeld MJ, Driscoll SP, Dominguez B, et al. (2015). Loss of motoneuron-specific microRNA-218 causes systemic neuromuscular failure. Science 350, 1525–1529. [PubMed: 26680198]

Amin ND, Senturk G, Costaguta G, Driscoll S, O'Leary B, Bonanomi D, and Pfaff SL (2021). A hidden threshold in motor neuron gene networks revealed by modulation of miR-218 dose. Neuron 109, 3252–3267.e6. [PubMed: 34450025]

Andreone BJ, Lacoste B, and Gu C (2015). Neuronal and vascular interactions. Annu. Rev. Neurosci 38, 25–46. [PubMed: 25782970]

Antipenko A, Himanen JP, van Leyen K, Nardi-Dei V, Lesniak J, Barton WA, Rajashankar KR, Lu M, Hoemme C, Püschel AW, et al. (2003). Structure of the semaphorin-3A receptor binding module. Neuron 39, 589–598. [PubMed: 12925274]

Bai G, Chivatakarn O, Bonanomi D, Lettieri K, Franco L, Xia C, Stein E, Ma L, Lewcock JW, and Pfaff SL (2011). Presenilin-dependent receptor processing is required for axon guidance. Cell 144, 106–118. [PubMed: 21215373]

Ballabio C, Anderle M, Gianesello M, Lago C, Miele E, Cardano M, Aiello G, Piazza S, Caron D, Gianno F, et al. (2020). Modeling medullo-blastoma in vivo and with human cerebellarorganoids. Nat. Commun 11, 583. [PubMed: 31996670]

Bonanomi D. (2019). Axon pathfinding for locomotion. Semin. Cell Dev. Biol 85, 26–35. [PubMed: 29141181]

Bonanomi D, Chivatakarn O, Bai G, Abdesselem H, Lettieri K, Marquardt T, Pierchala BA, and Pfaff SL (2012). Ret is a multifunctional coreceptor that integrates diffusible- and contact-axon guidance signals. Cell 148, 568–582. [PubMed: 22304922]

Bonanomi D, Valenza F, Chivatakarn O, Sternfeld MJ, Driscoll SP, Aslanian A, Lettieri K, Gullo M, Badaloni A, Lewcock JW, et al. (2019). p190RhoGAP filters competing signals to resolve axon guidance conflicts. Neuron 102, 602–620.e9. [PubMed: 30902550]

Carmeliet P, and Tessier-Lavigne M (2005). Common mechanisms of nerve and blood vessel wiring. Nature 436, 193–200. [PubMed: 16015319]

Cattin AL, Burden JJ, Van Emmenis L, Mackenzie FE, Hoving JJ, Garcia Calavia N, Guo Y, McLaughlin M, Rosenberg LH, Quereda V, et al. (2015). Macrophage-induced blood vessels guide Schwann cell-mediated regeneration of peripheral nerves. Cell 162, 1127–1139. [PubMed: 26279190]

Chen H, He Z, Bagri A, and Tessier-Lavigne M (1998). Semaphorin-neuropilin interactions underlying sympathetic axon responses to class III semaphorins. Neuron 21, 1283–1290. [PubMed: 9883722]

Choi Y, and Chan AP (2015). PROVEAN web server: a tool to predict the functional effect of amino acid substitutions and indels. Bioinformatics 31, 2745–2747. [PubMed: 25851949]

Christie SM, Hao J, Tracy E, Buck M, Yu JS, and Smith AW (2021). Interactions between semaphorins and plexin-neuropilin receptor complexes in the membranes of live cells. J. Biol. Chem 297, 100965. [PubMed: 34270956]

Conner DA (2001). Mouse embryo fibroblast (MEF) feeder cell preparation. Curr. Protoc. Mol. Biol Chapter 23. Unit 23 22.

D'Elia KP, and Dasen JS (2018). Development, functional organization, and evolution of vertebrate axial motor circuits. Neural Dev. 13, 10. [PubMed: 29855378]

Dessaud E, Yang LL, Hill K, Cox B, Ulloa F, Ribeiro A, Mynett A, Novitch BG, and Briscoe J (2007). Interpretation of the sonic hedgehog morphogen gradient by a temporal adaptation mechanism. Nature 450, 717–720. [PubMed: 18046410]

Dobin A, Davis CA, Schlesinger F, Drenkow J, Zaleski C, Jha S, Batut P, Chaisson M, and Gingeras TR (2013). STAR: ultrafast universal RNA-seq aligner. Bioinformatics 29, 15–21. [PubMed: 23104886]

Dodd J, and Jessell TM (1988). Axon guidance and the patterning of neuronal projections in vertebrates. Science 242, 692–699. [PubMed: 3055291]

Dray C, Rougon G, and Debarbieux F (2009). Quantitative analysis by in vivo imaging of the dynamics of vascular and axonal networks in injured mouse spinal cord. Proc. Natl. Acad. Sci. USA 106, 9459–9464. [PubMed: 19470644]

Efremova M, Vento-Tormo M, Teichmann SA, and Vento-Tormo R (2020). CellPhoneDB: inferring cell-cell communication from combined expression of multi-subunit ligand-receptor complexes. Nat. Protoc 15, 1484–1506. [PubMed: 32103204]

Eichmann A, and Brunet I (2014). Arterial innervation in development and disease. Sci. Transl. Med 6, 252ps259.

Ericson J, Thor S, Edlund T, Jessell TM, and Yamada T (1992). Early stages of motor neuron differentiation revealed by expression of homeobox gene Islet-1. Science 256, 1555–1560. [PubMed: 1350865]

Erskine L, François U, Denti L, Joyce A, Tillo M, Bruce F, Vargesson N, and Ruhrberg C (2017). VEGF-A and neuropilin 1 (NRP1)shape axon projections in the developing CNS via dual roles in neurons and blood vessels. Development 144, 2504–2516. [PubMed: 28676569]

Feiner L, Koppel AM, Kobayashi H, and Raper JA (1997). Secreted chick semaphorins bind recombinant neuropilin with similar affinities but bind different subsets of neurons in situ. Neuron 19, 539–545. [PubMed: 9331347]

Feiner L, Webber AL, Brown CB, Lu MM, Jia L, Feinstein P, Mombaerts P, Epstein JA, and Raper JA (2001). Targeted disruption of semaphorin 3C leads to persistent truncus arteriosus and aortic arch interruption. Development 128, 3061–3070. [PubMed: 11688556]

Fetcho JR (1987). A review of the organization and evolution of motoneurons innervating the axial musculature of vertebrates. Brain Res. 434, 243–280. [PubMed: 3300861]

Flanagan JG, and Leder P (1990). The kit ligand: a cell surface molecule altered in steel mutant fibroblasts. Cell 63, 185–194. [PubMed: 1698555]

Franze K, Janmey PA, and Guck J (2013). Mechanics in neuronal development and repair. Annu. Rev. Biomed. Eng 15, 227–251. [PubMed: 23642242]

Gaertner F, Reis-Rodrigues P, de Vries I, Hons M, Aguilera J, Riedl M, Leithner A, Tasciyan S, Kopf A, Merrin J, et al. (2022). WASp triggers mechanosensitive actin patches to facilitate immune cell migration in dense tissues. Dev. Cell 57, 47–62.e9. [PubMed: 34919802]

Gerber HP, Hillan KJ, Ryan AM, Kowalski J, Keller GA, Rangell L, Wright BD, Radtke F, Aguet M, and Ferrara N (1999). VEGF is required for growth and survival in neonatal mice. Development 126, 1149–1159. [PubMed: 10021335]

Gitler AD, Lu MM, and Epstein JA (2004). PlexinD1 and semaphorin signaling are required in endothelial cells for cardiovascular development. Dev. Cell 7, 107–116. [PubMed: 15239958]

Grima R (2007). Directed cell migration in the presence of obstacles. Theor. Biol. Med. Model 4, 2. [PubMed: 17227579]

Gu C, Rodriguez ER, Reimert DV, Shu T, Fritzsch B, Richards LJ, Kolodkin AL, and Ginty DD (2003). Neuropilin-1 conveys semaphorin and VEGF signaling during neural and cardiovascular development. Dev. Cell 5, 45–57. [PubMed: 12852851]

Gu C, Yoshida Y, Livet J, Reimert DV, Mann F, Merte J, Henderson CE, Jessell TM, Kolodkin AL, and Ginty DD (2005). Semaphorin 3E and plexin-D1 control vascular pattern independently of neuropilins. Science 307, 265–268. [PubMed: 15550623]

Hamm MJ, Kirchmaier BC, and Herzog W (2016). Sema3d controls collective endothelial cell migration by distinct mechanisms via Nrp1 and PlxnD1. J. Cell Biol 215, 415–30. [PubMed: 27799363]

Hao Y, Hao S, Andersen-Nissen E, Mauck WM 3rd, Zheng S, Butler A, Lee MJ, Wilk AJ, Darby C, Zager M, et al. (2021). Integrated analysis of multimodal single-cell data. Cell 184, 3573–3587.e29. [PubMed: 34062119]

Harrow J, Frankish A, Gonzalez JM, Tapanari E, Diekhans M, Kokocinski F, Aken BL, Barrell D, Zadissa A, Searle S, et al. (2012). GENCODE: the reference human genome annotation for the ENCODE Project. Genome Res. 22, 1760–1774. [PubMed: 22955987]

He P, Williams BA, Trout D, Marinov GK, Amrhein H, Berghella L, Goh ST, Plajzer-Frick I, Afzal V, Pennacchio LA, et al. (2020). The changing mouse embryo transcriptome at whole tissue and single-cell resolution. Nature 583, 760–767. [PubMed: 32728245]

Himmels P, Paredes I, Adler H, Karakatsani A, Luck R, Marti HH, Ermakova O, Rempel E, Stoeckli ET, and Ruiz de Almodóvar C (2017). Motor neurons control blood vessel patterning in the developing spinal cord. Nat. Commun 8, 14583. [PubMed: 28262664]

Ramón y Cajal S (1909). Histologie du systeme nerveux de l'homme et des vertébrés*1* (Maloine).

Huber W, Carey VJ, Gentleman R, Anders S, Carlson M, Carvalho BS, Bravo HC, Davis S, Gatto L, Girke T, et al. (2015). Orchestrating high-throughput genomic analysis with Bioconductor. Nat. Methods 12, 115–121. [PubMed: 25633503]

James JM, Gewolb C, and Bautch VL (2009). Neurovascular development uses VEGF-A signaling to regulate blood vessel ingression into the neural tube. Development 136, 833–841. [PubMed: 19176586]

James JM, and Mukouyama YS (2011). Neuronal action on the developing blood vessel pattern. Semin. Cell Dev. Biol 22, 1019–1027. [PubMed: 21978864]

Jessell TM (2000). Neuronal specification in the spinal cord: inductive signals and transcriptional codes. Nat. Rev. Genet 1, 20–29. [PubMed: 11262869]

Kisanuki YY, Hammer RE, Miyazaki J, Williams SC, Richardson JA, and Yanagisawa M (2001). Tie2-Cre transgenic mice: a new model for endothelial cell-lineage analysis in vivo. Dev. Biol 230, 230–242. [PubMed: 11161575]

Klose M, and Bentley D (1989). Transient pioneer neurons are essential for formation of an embryonic peripheral nerve. Science 245, 982–984. [PubMed: 2772651]

Kolodkin AL, and Tessier-Lavigne M (2011). Mechanisms and molecules of neuronal wiring: a primer. Cold Spring Harb. Perspect. Biol 3.

Lakso M, Pichel JG, Gorman JR, Sauer B, Okamoto Y, Lee E, Alt FW, and Westphal H (1996). Efficient in vivo manipulation of mouse genomic sequences at the zygote stage. Proc. Natl. Acad. Sci. USA 93, 5860–5865. [PubMed: 8650183]

Landmesser L (1978). The development of motor projection patterns in the chick hind limb. J. Physiol 284, 391–414. [PubMed: 731552]

Larina IV, Shen W, Kelly OG, Hadjantonakis AK, Baron MH, and Dickinson ME (2009). A membrane associated mCherry fluorescent reporter line for studying vascular remodeling and cardiac function during murine embryonic development. Anat. Rec, 292 (Hoboken), pp. 333–341.

Lee SK, Jurata LW, Funahashi J, Ruiz EC, and Pfaff SL (2004). Analysis of embryonic motoneuron gene regulation: derepression of general activators function in concert with enhancer factors. Development 131, 3295–3306. [PubMed: 15201216]

Lee WP, Stromberg MP, Ward A, Stewart C, Garrison EP, and Marth GT (2014). MOSAIK: a hash-based algorithm for accurate next-generation sequencing short-read mapping. PLoS One 9, e90581. [PubMed: 24599324]

Lewcock JW, Genoud N, Lettieri K, and Pfaff SL (2007). The ubiquitin ligase Phr1 regulates axon outgrowth through modulation of microtubule dynamics. Neuron 56, 604–620. [PubMed: 18031680]

Liao Y, Smyth GK, and Shi W (2014). featureCounts: an efficient general purpose program for assigning sequence reads to genomic features. Bioinformatics 30, 923–930. [PubMed: 24227677]

Liu X, Uemura A, Fukushima Y, Yoshida Y, and Hirashima M (2016). Semaphorin 3G provides a repulsive guidance cue to lymphatic endothelial cells via Neuropilin-2/PlexinD1. Cell Rep. 17, 2299–2311. [PubMed: 27880905]

Love CA, Harlos K, Mavaddat N, Davis SJ, Stuart DI, Jones EY, and Esnouf RM (2003). The ligand-binding face of the semaphorins revealed by the high-resolution crystal structure of SEMA4D. Nat. Struct. Biol 10, 843–848. [PubMed: 12958590]

Love MI, Huber W, and Anders S (2014). Moderated estimation of fold change and dispersion for RNA-seq datawith DESeq2. Genome Biol. 15, 550. [PubMed: 25516281]

Madugundu AK, Na CH, Nirujogi RS, Renuse S, Kim KP, Burns KH, Wilks C, Langmead B, Ellis SE, Collado-Torres L, et al. (2019). Integrated transcriptomic and proteomic analysis of primary human umbilical vein endothelial cells. Proteomics 19, e1800315. [PubMed: 30983154]

Mehta V, Pang KL, Rozbesky D, Nather K, Keen A, Lachowski D, Kong Y, Karia D, Ameismeier M, Huang J, et al. (2020). The guidance receptor plexin D1 is a mechanosensor in endothelial cells. Nature 578, 290–295. [PubMed: 32025034]

Mukouyama YS, Gerber HP, Ferrara N, Gu C, and Anderson DJ (2005). Peripheral nerve-derived VEGF promotes arterial differentiation via neuropilin 1-mediated positive feedback. Development 132, 941–952. [PubMed: 15673567]

Mumblat Y, Kessler O, Ilan N, and Neufeld G (2015). Full-length Semaphorin-3C is an inhibitor of tumor lymphangiogenesis and metastasis. Cancer Res. 75, 2177–2186. [PubMed: 25808871]

Muramatsu R, Takahashi C, Miyake S, Fujimura H, Mochizuki H, and Yamashita T (2012). Angiogenesis induced by CNS inflammation promotes neuronal remodeling through vessel-derived prostacyclin. Nat. Med 18, 1658–1664. [PubMed: 23042236]

Murphy DA, and Courtneidge SA (2011). The ‘ins’ and ‘outs’ of podosomes and invadopodia: characteristics, formation and function. Nat. Rev. Mol. Cell Biol 12,413–26. [PubMed: 21697900]

Nichols EL, and Smith CJ (2019). Pioneer axons employ Cajal’s battering ram to enter the spinal cord. Nat. Commun 10, 562. [PubMed: 30718484]

Oh WJ, and Gu C (2013). The role and mechanism-of-action of Sema3E and Plexin-D1 in vascular and neural development. Semin. Cell Dev. Biol 24, 156–162. [PubMed: 23270617]

Palikuqi B, Nguyen DT, Li G, Schreiner R, Pellegata AF, Liu Y, Redmond D, Geng F, Lin Y, Gómez-Salinero JM, et al. (2020). Adaptable haemodynamic endothelial cells for organogenesis and tumorigenesis. Nature 585, 426–32. [PubMed: 32908310]

Plein A, Calmont A, Fantin A, Denti L, Anderson NA, Scambler PJ, and Ruhrberg C (2015). Neural crest-derived SEMA3C activates endothelial NRP1 for cardiac outflow tract septation. J. Clin. Invest 125, 2661–2676. [PubMed: 26053665]

Ruiz de Almodovar C, Fabre PJ, Knevels E, Coulon C, Segura I, Haddick PC, Aerts L, Delattin N, Strasser G, Oh WJ, et al. (2011). VEGF mediates commissural axon chemoattraction through its receptor Flk1. Neuron 70, 966–978. [PubMed: 21658588]

Santiago-Medina M, Gregus KA, Nichol RH, O'Toole SM, and Gomez TM (2015). Regulation of ECM degradation and axon guidance by growth cone invadosomes. Development 142, 486–496. [PubMed: 25564649]

Sanyas I, Bozon M, Moret F, and Castellani V (2012). Motoneuronal Sema3C is essential for setting stereotyped motor tract positioning in limb-derived chemotropic semaphorins. Development 139, 3633–3643. [PubMed: 22899844]

Skene NG, and Grant SGN (2016). Identification of Vulnerable Cell Types in Major Brain Disorders Using Single Cell Transcriptomes and Expression Weighted Cell Type Enrichment. Frontiers in Neuroscience 10, 16. 10.3389/fnins.2016.00016. [PubMed: 26858593]

Smith T, Heger A, and Sudbery I (2017). UMI-tools: modeling sequencing errors in Unique Molecular Identifiers to improve quantification accuracy. Genome Res. 27, 491–499. [PubMed: 28100584]

Suter TACS, and Jaworski A (2019). Cell migration and axon guidance at the border between central and peripheral nervous system. Science 365.

Tabas-Madrid D, Nogales-Cadenas R, and Pascual-Montano A (2012). GeneCodis3: a non-redundant and modular enrichment analysis tool for functional genomics. Nucleic Acids Res. 40, W478–W483. [PubMed: 22573175]

Tam SJ, and Watts RJ (2010). Connecting vascular and nervous system development: angiogenesis and the blood-brain barrier. Annu. Rev. Neurosci 33, 379–408. [PubMed: 20367445]

Thaler J, Harrison K, Sharma K, Lettieri K, Kehrl J, and Pfaff SL (1999). Active suppression of interneuron programs within developing motor neurons revealed by analysis of homeodomain factor HB9. Neuron 23, 675–687. [PubMed: 10482235]

Torres-Vázquez J, Gitler AD, Fraser SD, Berk JD, Van NP, Fishman MC, Childs S, Epstein JA, and Weinstein BM (2004). Semaphorin-plexin signaling guides patterning of the developing vasculature. Dev. Cell 7, 117–123. [PubMed: 15239959]

Tosney KW, and Landmesser LT (1985a). Development of the major pathways for neurite outgrowth in the chick hindlimb. Dev. Biol 109, 193–214. [PubMed: 2985457]

Tosney KW, and Landmesser LT (1985b). Growth cone morphology and trajectory in the lumbosacral region of the chick embryo. J. Neurosci 5, 2345–2358. [PubMed: 4032000]

Toyofuku T, Yabuki M, Kamei J, Kamei M, Makino N, Kumanogoh A, and Hori M (2007). Semaphorin-4A, an activator for T-cell-mediated immunity, suppresses angiogenesis via Plexin-D1. EMBO J. 26, 1373–1384. [PubMed: 17318185]

Wu S, Wu Y, and Capecchi MR (2006). Motoneurons and oligodendrocytes are sequentially generated from neural stem cells but do not appear to share common lineage-restricted progenitors in vivo. Development 133, 581–590. [PubMed: 16407399]

Xie Z, Bailey A, Kuleshov MV, Clarke DJB, Evangelista JE, Jenkins SL, Lachmann A, Wojciechowicz ML, Kropiwnicki E, Jagodnik KM, et al. (2021). Gene set knowledge discovery with Enrichr. Curr. Protoc 1, e90. [PubMed: 33780170]

Yang WJ, Hu J, Uemura A, Tetzlaff F, Augustin HG, and Fischer A (2015). Semaphorin-3C signals through Neuropilin-1 and PlexinD1 receptors to inhibit pathological angiogenesis. EMBO Mol. Med 7, 1267–1284. [PubMed: 26194913]

Yusa K, Zhou L, Li MA, Bradley A, and Craig NL (2011). A hyperactive piggyBac transposase for mammalian applications. Proc. Natl. Acad. Sci. USA 108, 1531–1536. [PubMed: 21205896]

Zang Y, Chaudhari K, and Bashaw GJ (2021). New insights into the molecular mechanisms of axon guidance receptor regulation and signaling. Curr. Top. Dev. Biol 142, 147–196. [PubMed: 33706917]

Zhang Y, Parmigiani G, and Johnson WE (2020). ComBat-seq: batch effect adjustment for RNA-seq count data. NAR Genom. Bioinform 2, lqaa078. [PubMed: 33015620]

Zhang Y, Singh MK, Degenhardt KR, Lu MM, Bennett J, Yoshida Y, and Epstein JA (2009). Tie2Cre-mediated inactivation of plexinD1 results in congenital heart, vascular and skeletal defects. Dev. Biol 325, 82–93. [PubMed: 18992737]

Highlights

- Plexin-D1 is required in ECs to establish axial MN connectivity
- MNs release attractive and repulsive signals that pattern blood vessels
- Motor axons displace endothelial obstacles with Sema3C/Plexin-D1 signaling
- Neurovascular crosstalk links axon targeting of neuronal subtypes to vascularization

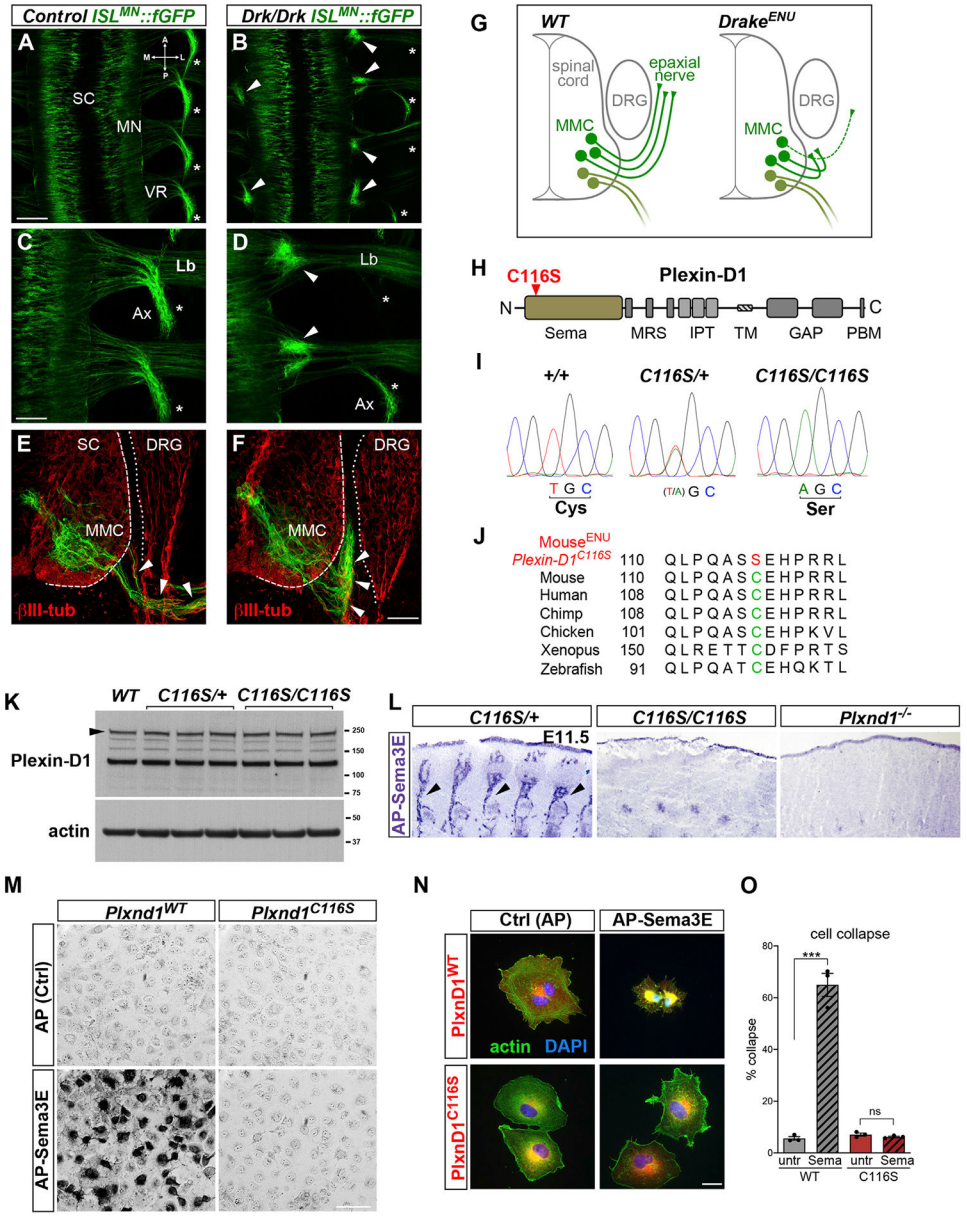

Figure 1. The ENU-induced Plexin-D1 allele Drake causes selective motor axon guidance defects

(A–D) Whole mounts of E12.5 *ISL^MN::fGFP^+* embryos (dorsal view of lumbar region). MNs in the spinal cord (SC) project through the ventral roots (VRs) to epaxial (Ax, asterisks) or limb (Lb) muscles. Drake homozygotes (*Drk/Drk*) display proximal motor axon bundles (arrowheads) and corresponding depletion of epaxial nerves. Control is *Drk/+*. Other nerve tracts are intact. A, anterior; P, posterior; M, medial; L, lateral.

(E and F) E12.5 transverse sections show the initial course of *ISL^MN::fGFP^+* epaxial motor axons (arrowheads in E), which is halted in *Drake* mutants (arrowheads in F). βIII-tubulin, pan-neuronal marker. *ISL^MN::fGFP* signal is higher in the MMC neurons relative to other subtypes. DRG, dorsal root ganglia.

(G) Motor axon stalling in *Drake* embryo.

(H) Plexin-D1 with C116S mutation in “Sema” ligand-binding domain. Other domains are labeled.
(I) Genomic DNA sequencing reveals homozygous T>A substitution in *Plxnd1* exon 1 of *Drake* embryos, leading to C116S mutation.
(J) Evolutionary conservation of C116 (green, mouse sequence) and ENU-induced mutation (red).
(K) Lysates of E12.5 spinal cords and surrounding tissue. Plexin-D1 levels in *Drake* homozygous (*C116S/C116S*) or heterozygous (*C116S/+*) mutants are comparable to WT. Actin is a loading control.
(L) Alkaline phosphatase (AP)-tagged Sema3E reveals Plexin-D1 in E11.5 sagittal sections. Arrows point to intersomitic vessels. Binding is absent in *C116S/C116S* and *Plxnd1* KO embryos.
(M) AP-Sema3E binding to COS-7 cells expressing WT Plexin-D1 but not C116S mutant. No signal is detected with control AP-Fc.
(N) Sema3E induces collapse of COS-7 cells expressing WT Plexin-D1 but not C116S mutant.
(O) Quantification of cell collapse. Mean ± SEM, Unpaired t test (***) p = 0.0002 WT untreated (untr.) versus Sema; (ns) p = 0.24 C116 untr. versus Sema. Sample size for this and following quantification is reported in STAR Methods.
Scale bars: 200 μm in (A) and (B); 100 μm in (C) and (D); 50 μm in (E) and (F); 50 μm in (M); and 50 μm in (N).
See also Figure S1.

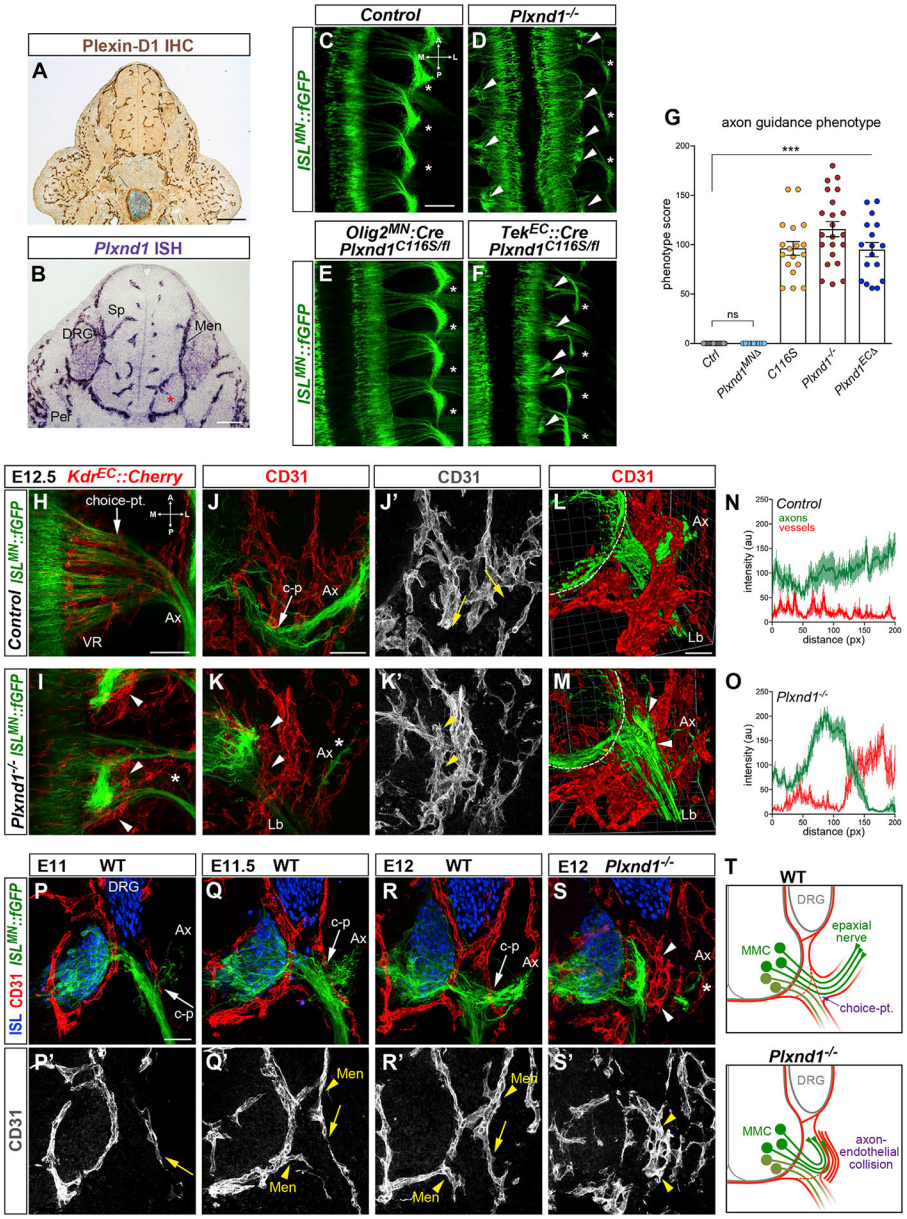

Figure 2. Endothelial Plexin-D1 is required for motor axon guidance and interaction with vessels

(A) Immunohistochemistry for Plexin-D1 reveals restricted vascular expression at E11.5.

(B) *In situ* hybridization at E11.5 detects *Plexin-D1* on blood vessels in the spinal cord (Sp), meninges (Men) and peripheral tissues (Per), but not in the MC (asterisk). Lower signal is visible in DRG.

(C–F) Aberrant motor axon bundles (arrowheads) and epaxial nerve thinning (asterisks) in E12.5 $Plxnd1^{-/-}$ whole mounts (dorsal view) (D) and following deletion of *Plxnd1* from ECs (Tek^{EC}*::Cre;* $Plxnd1^{C116S/fl}$) (F) but not MNs ($Olig2^{MN}$*::Cre;* $Plxnd1^{C116S/fl}$) (E). Control is $Olig2^{MN}$*::Cre;* $Plxnd1^{+/fl}$.

(G) Quantification of axon guidance phenotype. Mean ± SEM, ANOVA/Dunnett's test (***) $p < 0.00001$ C116S, $Plxnd1^{-/-}$ and $Plxnd1^{EC\Delta}$ versus *Ctrl*; (ns) $Plxnd1^{MN\Delta}$ versus *Ctrl*; ANOVA/Tukey's test (ns) $p > 0.1$ *C116S* versus $Plxnd1^{-/-}$ versus $Plxnd1^{EC\Delta}$.

(H and I) Whole mounts of embryos co-expressing motor (*ISL^{MN}::fGFP*) and endothelial (*Kdk^{EC}::Cherry*) reporters (E12.5, dorsal view). Arrow marks the MMC choice point. Ectopically arranged ECs surround axon bundles in *Plxnd1$^{-/-}$* (arrowheads in I). Epaxial nerves (Ax) are depleted (asterisk).

(J–K′) MMC axons (*ISL^{MN}::fGFP^{high}*) extend through vessels (CD31^{+}) in E12.5 controls (J and J′; c-p, MMC choice point). Axons are blocked by ectopic EC clusters in mutants (K and K′, arrowheads) resulting in near-ablation of epaxial nerves (Ax, asterisk). Lb, limb nerve (*ISL^{MN}::fGFP^{low}*).

(L and M) 3D two-photon imaging (E12.5). The rendered volume was clipped in M to visualize axon-EC apposition (arrowheads). Dashed lines mark the spinal cord margin.

(N and O) Intensity profile of *ISL^{MN}::fGFP* (motor axons) and CD31 (vessels) along MMC trajectory reveals abnormal adjacent peaks in mutants (mean ± SEM).

(P–S′) Lumbar transverse sections of *ISL^{MN}::fGFP^{+}* embryos stained for endothelial marker CD31 and motor/sensory neuron marker Isl1/2. MMC projections (Ax) intersect ECs migrating from the meninges (Men, arrowheads in Q′ and R′) along the common nerve path. Epaxial choice point (c-p, arrows in P–R′) In *Plxnd1$^{-/-}$*, axons stall against ectopic EC clusters (arrowheads in S and S′). Asterisk marks residual epaxial axons.

(T) MMC axons are obstructed by ECs in *Plxnd1* mutants. To simplify the diagram of axonal projections, MMC cell bodies are shown in a fictitious lateral position.

Scale bars: 200 μm in (A); 100 μm in (B); 200 μm in (C)–(F); 100 μm in (H) and (I); 50 μm in (J)–(K′); 50 μm in (L) and (M); and 50 μm in (P)–(S′).

See also Figure S2.

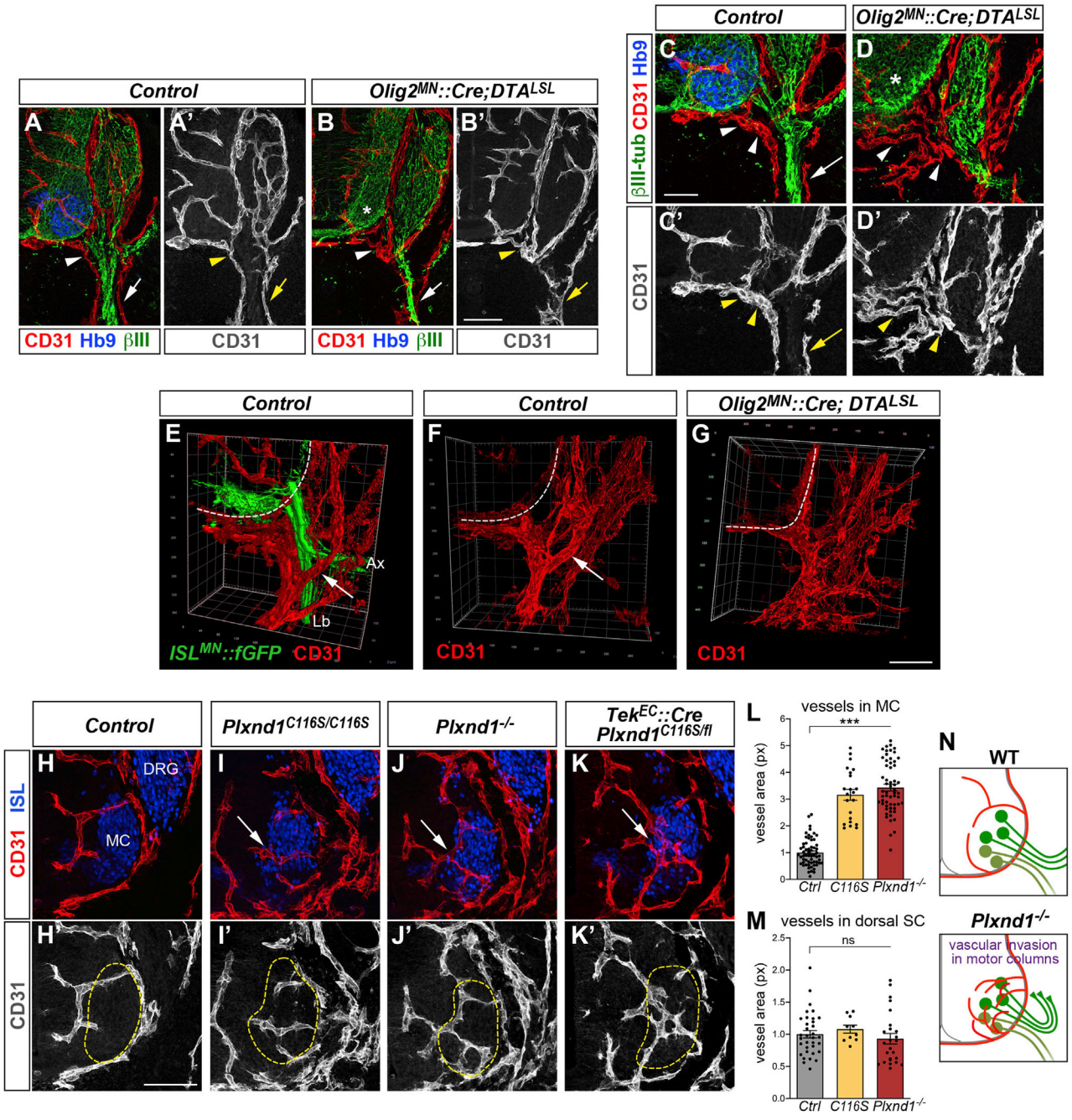

Figure 3. Motor-endothelial interactions instruct vascular patterning in the spinal cord and ventral root

(A–D′) Genetic ablation of MNs in E12 *Olig2^{MN}::Cre; DTA^{LSL}* embryos disrupts vascular patterns at motor exit points (arrowheads) and along sensory fibers (βIII-tubulin, arrows). Controls are Cre negative. MNs (Hb9^{+}) are efficiently eliminated (asterisks in B and D). (E–G) 3D view of vessels surrounding *ISL^{MN}::fGFP^{+}* motor nerves in E12 controls (arrows in E and F). This configuration is disrupted in absence of motor projections (G). Ax, epaxial nerve; Lb, limb nerve.

(H–K′) Vascular invasion of MCs (Isl1/2^{+}, dashed lines) in *Plxnd1* mutants (E12.5, lumbar level). Vessels encircle MCs in controls ($^{Plxnd1^{+/-}}$, H and H′) but intermingle with MNs in mutants (I–K′, arrows).

(L) Quantification ofvascular area (CD31 + px) within MCs at lumbar level. Mean, normalized to control ± SEM, ANOVA/Dunnett's test (***) $p < 0.00001$ C116S and Plxnd1~'~ versus Ctrl.

(M) Quantification of vascular area (CD31^{+} px) in dorsal spinal cord. Mean, normalized to control ± SEM, ANOVA/Dunnett's test (ns) $p > 0.5$.

(N) Vascular invasion of MCs in *Plxnd1* mutants.

Scale bars: 100 μm in (A)–(B′); 50 μm in (C)–(D′); 100 μm in (E)–(G); and 100 μm in (H)μ(K′).

See also Figure S3.

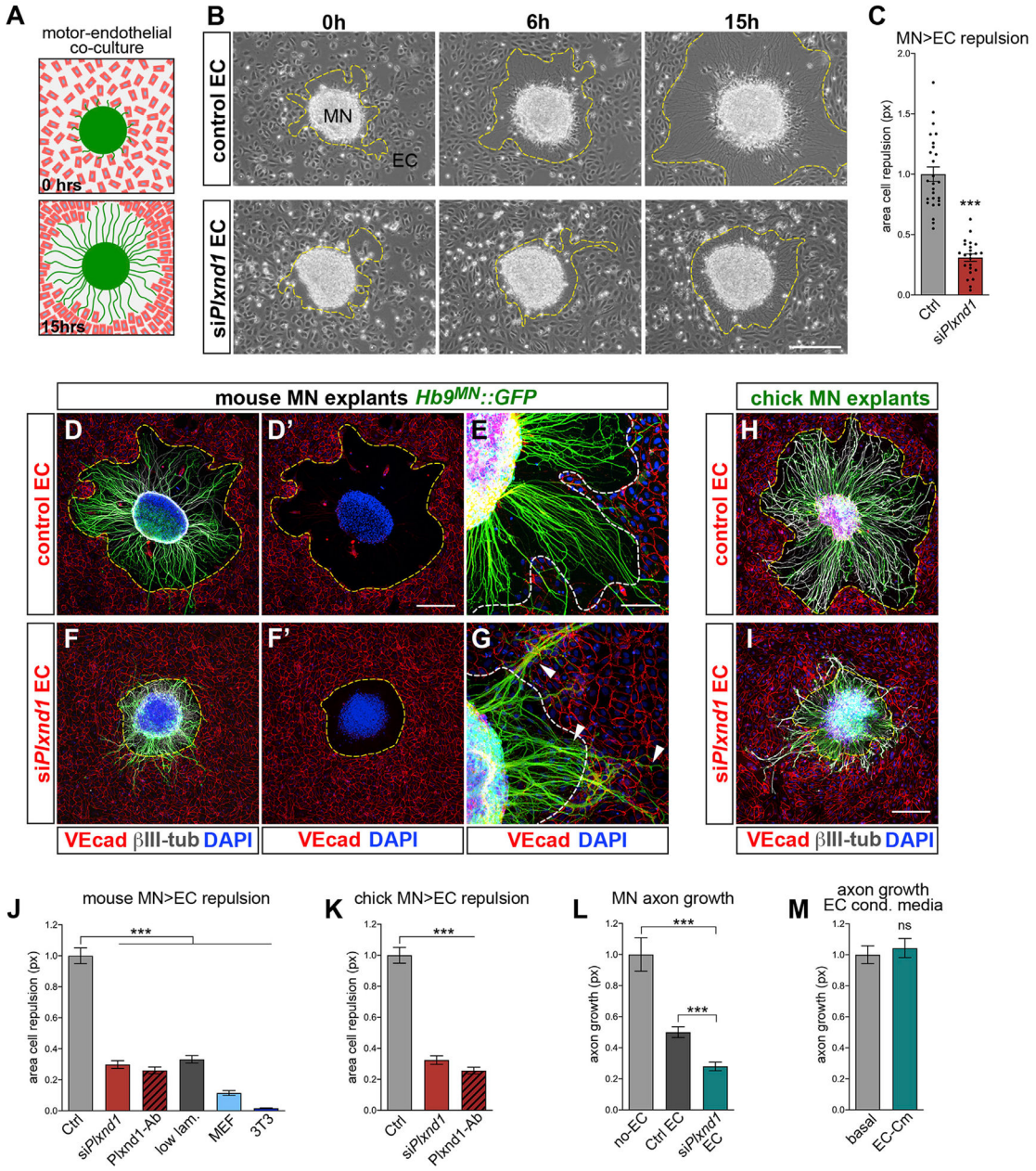

Figure 4. Plexin-D1 is required for EC repulsion by motor axons

(A) MN explant-EC repulsion assay.

(B) Live imaging of MN-EC co-cultures. (Top panels) HUVECs (EC) settle next to explants (0 h) but are repelled as axons extend. Dashed lines here and in following panels mark the EC front. (Bottom panels) *Plxnd1* KD from ECs (si*Plxnd1* EC) affects repulsion. “Control EC” transfected with non-targeting siRNA.

(C) EC repulsion quantified by measuring cell-free area after overnight (ON) growth. Mean, normalized to control ± SEM, Unpaired t test (***) $p < 0.0001$.

(D–G) ON co-cultures between *Hb9*^{MN}*::GFP* motor explants and control (D and E) or si*Plxnd1* EC (F and G) stained for EC marker VE-cadherin (VEcad) and neuronal βIII-tubulin.

(H and I) Co-cultures between motor explants from chick neural tube electroporated with GFP (green) and either control (H) or si*Plxnd1* EC (I).

(J) EC repulsion after ON co-culture with mouse motor explants. “Control”: HUVEC WT or transfected with non-targeting siRNA; “si*Plxnd1*”: *Plxnd1* KD; “anti-Plxnd1”: blocking antibody; “low-laminin” substrate; “MEF”/“3T3”: co-cultures with primary mouse embryonic fibroblasts or NIH-3T3. Mean, normalized to control ± SEM, ANOVA/Dunnett’s multiple comparison test (***) $p < 0.0001$ versus control.

(K) EC repulsion in co-cultures with chick motor explants. Mean, normalized to control ± SEM, ANOVA/Dunnett’s multiple comparison test (***) $p < 0.0001$ versus control.

(L) Axon extension from *Hb9*^{MN}*::GFP* motor explants cultured alone or with either control or si*Plxnd1* EC. Mean, normalized to control ± SEM, ANOVA/Dunnett’s test (***) $p < 0.0001$ versus control; unpaired t test (***) $p < 0.0001$ si*Plxnd1* versus control.

(M) MN explants cultured with HUVEC-conditioned media versus control basal media. Mean, normalized to control ± SEM, Unpaired t test (ns) $p = 0.61$.

Scale bars: 200 μm in (B); 200 μm in (F) and (F’); 100 μm in (E) and (G); and 200 μm.

See also Figure S4 and Videos S1, S2, S3, S4, S5, and S6.

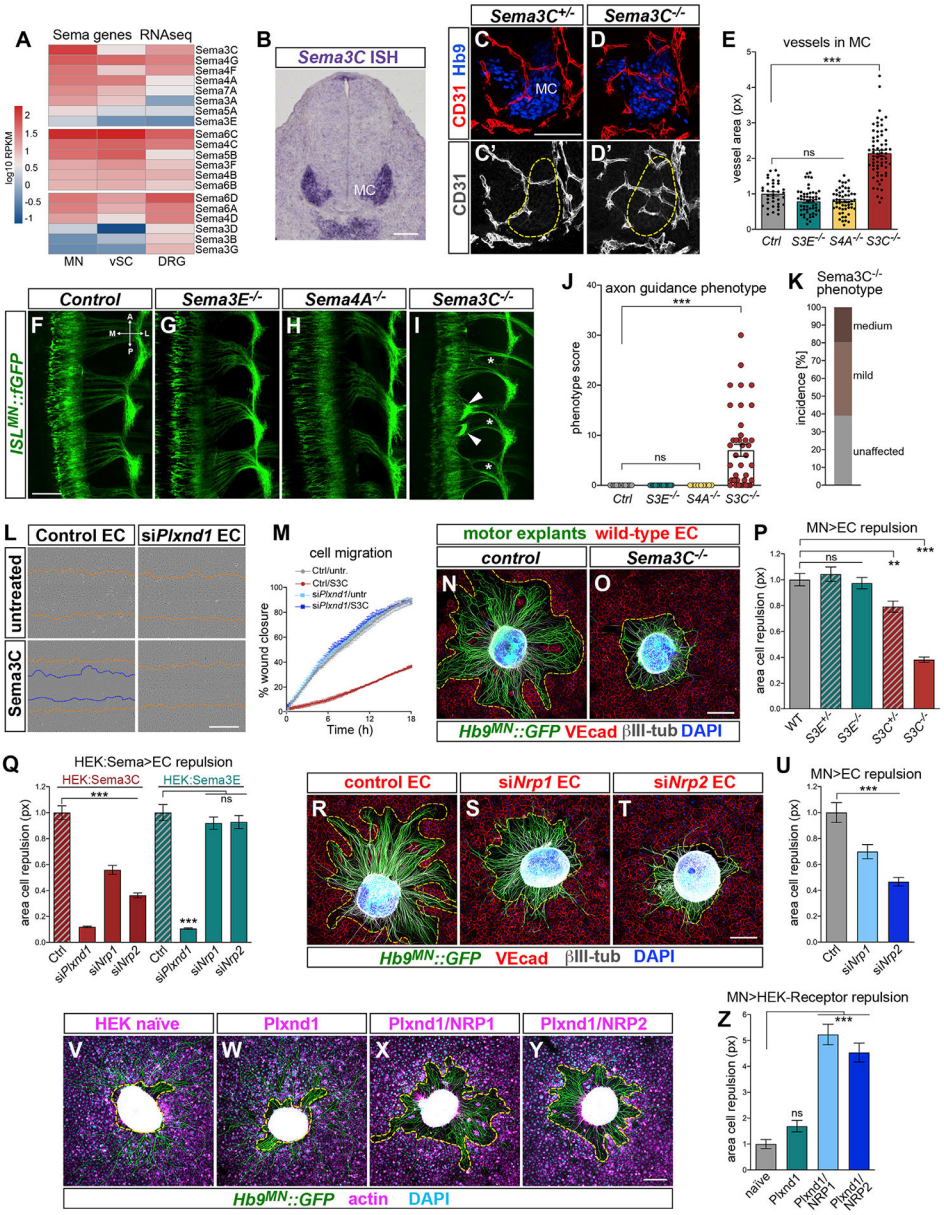

Figure 5. MN-derived Sema3C triggers EC repulsion through Plexin-D1/NRP receptors

(A) Normalized RNA-seq counts for Semaphorins in *Hb9*^{MN}*::GFP*$^{+}$ MNs, GFP~ spinal cord cells (vSC) and DRG FACS-purified from E12.5 embryos. *Sema3C* is high in MNs while *Sema3E* levels are negligible.

(B) *Sema3C* detected in MCs by *in situ* hybridization at E11.5.

(C–D′) Vessels invade MCs (Hb9^{+}, outlined) in *Sema3C*$^{-/-}$ (D and D′) but avoid this region in controls (*Sema3C*$^{+/-}$, C and C′; E12.5 lumbar transverse sections).

(E) Quantification of vascular area (CD31^{+} px) within MCs. Mean, normalized to control ± SEM, ANOVA/Dunnett's test (***) $p < 0.00001$ *Sema3C*$^{-/-}$ versus *Ctrl*; (ns) $p > 0.1$ *Sema3E*$^{-/-}$ and *Sema4A*$^{-/-}$ versus *Ctrl*.

(F–I) Proximal axon bundling (arrowheads) and epaxial nerve thinning (asterisks) in *Sema3C*$^{-/-}$ whole mounts (E12.5, dorsal view). *Sema3E* and *Sema4A* mutants are unaffected. Control is *Sema3C* heterozygous.

(J) Quantification of axon guidance phenotype. Mean ± SEM, ANOVA/Dunnett's test (***) p = 0.0002 *Sema3C*$^{-/-}$ versus *Ctrl*; (ns) *Sema3E*$^{-/-}$ and *Sema4A*$^{-/-}$ versus Ctrl.

(K) Penetrance and severity of axon guidance defects in *Sema3C* mutants.

(L) Last frames (18 h) of scratch wound healing assay on control (siCtrl-transfected) or *Plxnd1* KD HUVEC stimulated with Sema3C (lower panels) or left untreated (upper panels). Orange lines mark the initial wound margin; blue lines mark the migratory front. Both untreated control and si*Plxnd1* EC migrate to close the gap. Sema3C inhibits migration of control but not si*Plxnd1* EC.

(M) HUVEC migration rate in scratch assay. Mean ± SEM (see also Figure S5H).

(N and O) *Hb9*^{MN}*::GFP* motor explants from either WT (N) or *Sema3C*$^{-/-}$ embryos (O) cultured ON with HUVEC.

(P) Quantification of EC repulsion in co-cultures with *Sema3E* or *Sema3C* KO motor explants. Repulsion from *Sema3C* heterozygous and KO explants (but not *Sema3E*$^{-/-}$) is blunted. Mean, normalized to WT ± SEM, ANOVA/Dunnett's test (***) p < 0.0001 *Sema3C*$^{-/-}$ versus *Ctrl*; (**) p = 0.0046 $^{Sema3C^{+/\sim}}$ versus *Ctrl*; (ns) p > 0.8 *Sema3E*$^{+/\sim}$ and *Sema3E*$^{-/-}$ versus *Ctrl*.

(Q) Quantification of HUVEC repulsion from HEK cells overexpressing Sema3E (HEK:SemaE) or Sema3C (HEK:Sema3C). Representative images are shown in Figure S5P. *Plxnd1* KD in HUVEC prevents repulsion from Sema3E and Sema3C. *Nrp1* or *Nrp2* KD impairs repulsion from Sema3C but not Sema3E. Mean, normalized to WT ± SEM, ANOVA/Dunnett's test for HEK:Sema3C (***) p < 0.0001 si*Plxnd1*, si*Nrp1*, si*Nrp2* versus Ctrl; for HEK:Sema3E (***) p < 0.0001 si*Plxnd1* versus *Ctrl*; (ns) p > 0.5 si*Nrp1*, si*Nrp2* versus Ctrl.

(R–T) Co-cultures between *Hb9*^{MN}*::GFP* motor explants and control HUVEC (R) or HUVEC with KD of either Nrp1 (S) or *Nrp2* (T).

(U) Silencing *Nrp1* and *Nrp2* impairs EC repulsion. Mean, normalized to WT ± SEM, ANOVA/Dunnett's test (***) p = 0.0005 si*Nrp1* versus Ctrl; (***) p < 0.0001 si*Nrp2* versus *Ctrl*.

(V–Y) Co-cultures between motor explants and naive HEKs (V) or cells stably transfected with Plexin-D1 alone (W) or in combination with either NRP1 (Plxnd1/NRP1) (X) or NRP2 (Plxnd1/NRP2) (Y). HEKs are identified by F-actin (magenta) and nuclear (DAPI, cyan) staining. Motor axons grow over HEK-Ctrl and HEK-Plxnd1 but repel cells co-expressing Plexin-D1/NRPs. Dashed lines mark cell-free area.

(Z) Quantification of HEK cell repulsion. Mean, normalized to WT ± SEM, ANOVA/Dunnett's test (***) p < 0.0001 *Plxnd1/Nrp1* and *Plxnd1/Nrp2* versus Ctrl; (ns) p = 0.44 *Plxnd1* versus *Ctrl*.

Scale bars: 100 μm in (B); 100 μm in (C)x–(D'); 200 μm in (F)–(I); 400 μm in (L); 200 μm in (N)–(O); 200 μm in (R)–(T); and 200 μm in (V)–(Y).

See also Figure S5.

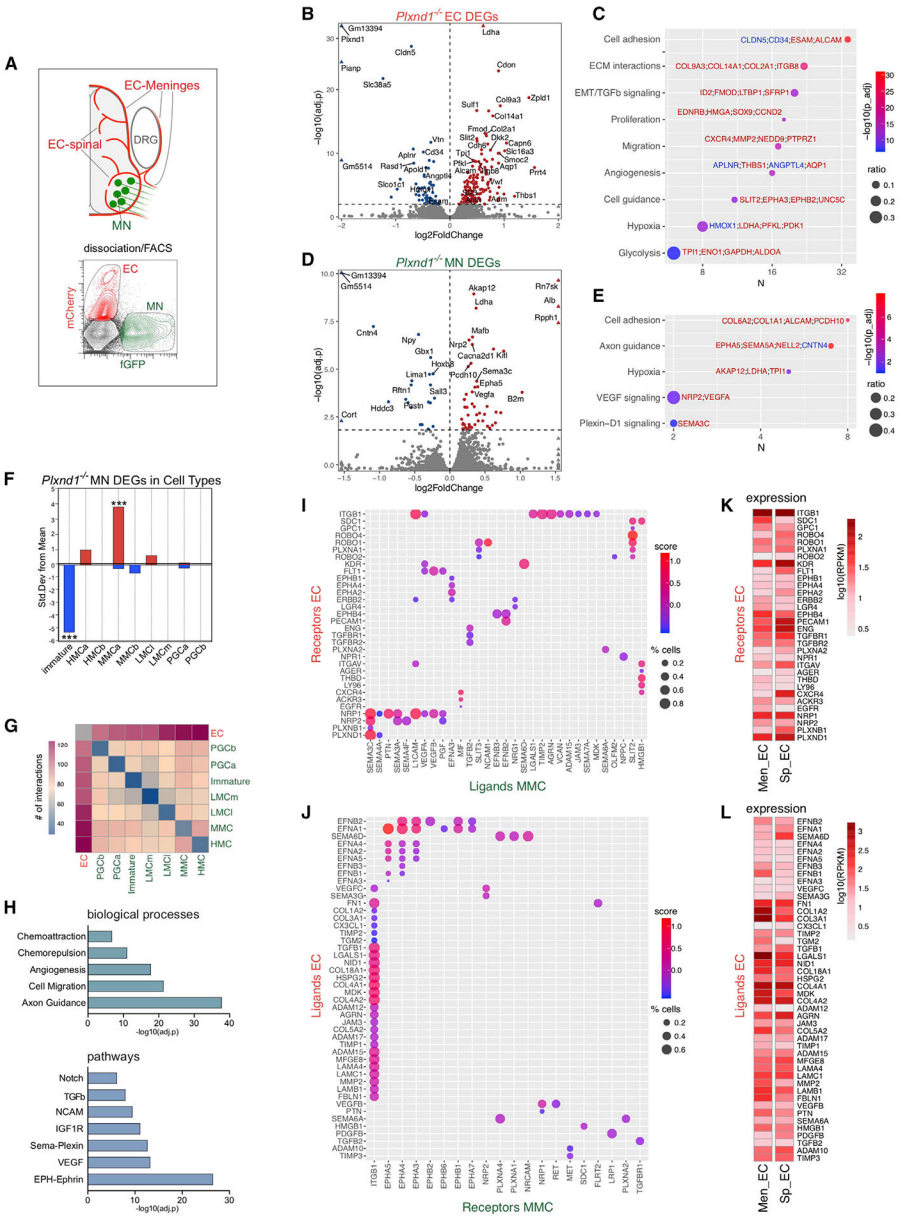

Figure 6. Mutual signaling underlying MN-EC crosstalk

(A) ECs (from spinal and meningeal vasculature) and MNs were FACS-purified from E12.5 embryos expressing *ISL*^{MN}*::fGFP*$^{+}$*/Kdr*^{EC}*::Cherry* reporters and analyzed by RNA-seq.

(B) Volcano plot of genes upregulated (160, red) or downregulated (65, blue) in *Plxnd1*$^{-/-}$ ECs (adjusted $p < 0.01$). Selected DEGs with highest significance are labeled.

(C) Gene ontology (GO) enrichment of DEGs in *Plxnd1*$^{-/-}$ ECs (*Plxnd1* was removed). Dot plot shows the number of genes associated with GO term (x axis), gene count ratio (circle size) and enrichment significance (color scale). Selected upregulated (red) and downregulated (blue) genes are shown.

(D) Volcano plot of genes upregulated (52, red) or downregulated (23, blue) in MNs of *Plxnd1−/−* embryos (adjusted $p < 0.01$).

(E) GO enrichment of DEGs in MNs from *Plxnd1*$^{-/-}$ embryos.

(F) Stratification of *Plxnd1*$^{-/-}$ DEGs among MN subtypes by EWCE. Upregulated genes, red; downregulated genes, blue. (***) p = 0.0002 immature; p = 0.0005 MMCa.
(G) Counts of ligand-receptor interactions identified by CellPhoneDB between MN subtypes (E12.5) and ECs isolated from the mesenchyme of E11–E13 mouse embryos.
(H) GO of ligand-receptor pairs between MMC and EC identified by CellPhoneDB.
(I and J) Representation of the strongest ligand-receptor interactions between MMC and EC from a curated list of 675 pairs associated with cell guidance and angiogenesis. (I) Interactions between MMC ligands (31) and EC receptors (32). (J) Interactions between EC ligands (46) and MMC receptors (20). Color scale, “interaction scores.” Circle size, lowest percentage of cells of either type expressing a gene in the pair.
(K and L) Expression of receptors (K) and ligands (L) measured by RNA-seq of ECs isolated from either the meninges (Men_EC) or spinal cord (Sp_EC) of E12.5 embryos. Several ligands were higher in Men_ECs (20/46; adjusted p < 0.001) including ephrins and ECM factors. Most of these genes were expressed in HUVECs (Table S5).
See also Figure S6 and Tables S1, S2, S3, S4, and S5.

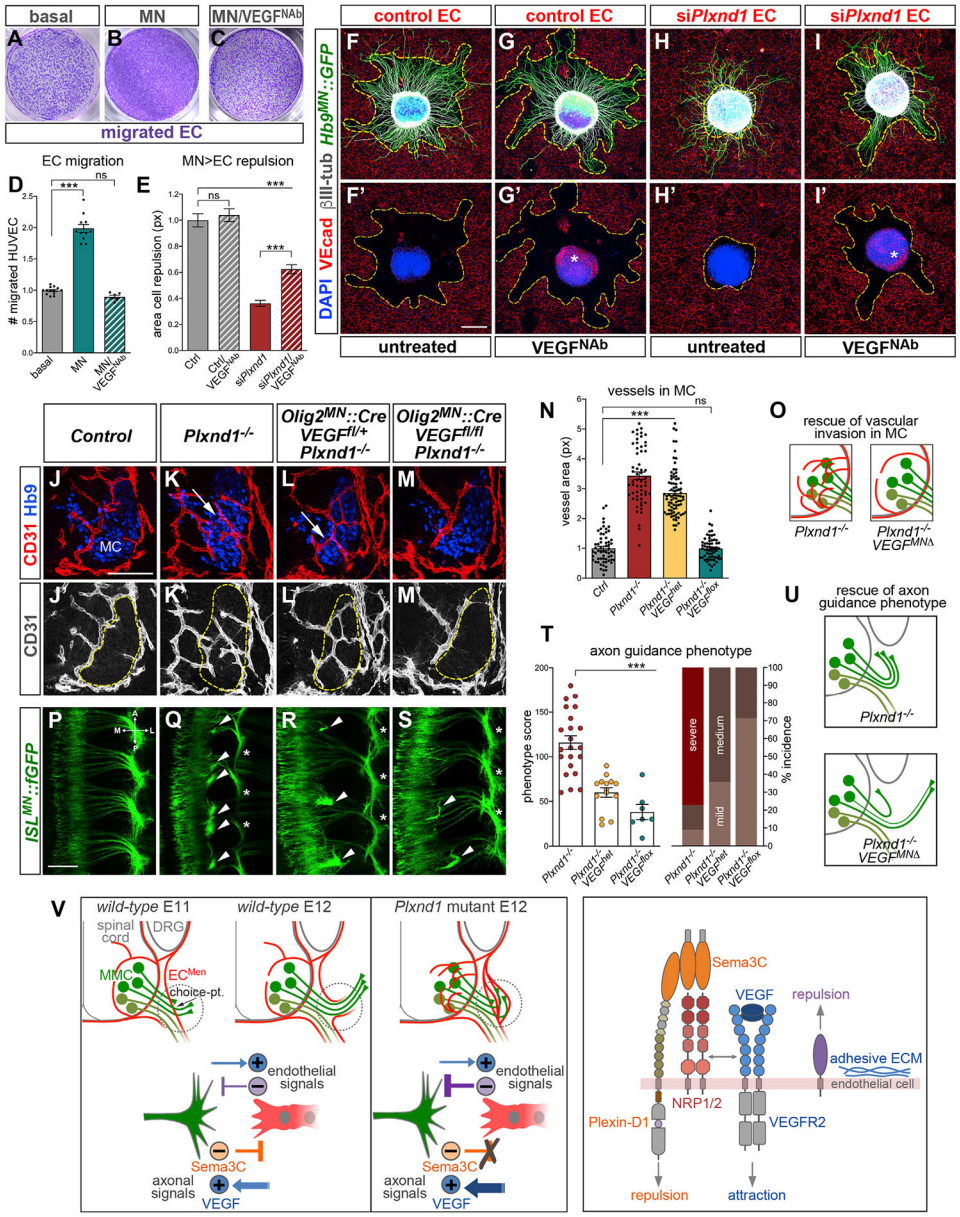

Figure 7. Integration of opposing motor-derived stimuli by ECs controls axon targeting and SC vascularization

(A–C) Crystal violet staining of HUVECs migrated to the bottom side of Transwell membrane. Migration is stimulated by MN-conditioned media in the lower compartment (B) relative to control basal media (A). The effect is prevented by neutralizing anti-VEGF164 antibody (VEGF^{Nab}) added to the lower chamber during migration (6 h) (C).

(D) Quantification of HUVEC migration. Mean, normalized to Ctrl ± SEM, ANOVA/ Dunnett's test (***) $p < 0.0001$ MN versus basal; (ns) $p = 0.26$ MN/VEGF^{Nab} versus basal.

(E) Quantification of cell repulsion in co-cultures between WT motor explants and control or si*Pxlnd1* HUVECs either treated with VEGF^{NAb} or left untreated. *Plxnd1* KD (si*Plxnd1*) prevents repulsion, and this effect is partially reversed by VEGF blockade (si*Plxnd1*/ VEGF^{Nab}). VEGF^{Nab} does not affect repulsion of control cells (Ctrl/VEGF^{Nab}) compared

with co-cultures in basal media (Ctrl). Mean, normalized to Ctrl ± SEM, ANOVA/Dunnett's test (***) $p < 0.0001$ si*Plxnd1* and si*Plxnd1*/VEGF^{Nab} versus Ctrl; (ns) $p = 0.85$ Ctrl/VEGF^{Nab} versus Ctrl; unpaired t test (***) $p < 0.0001$ si*Plxnd1*/VEGF^{Nab} versus si*Plxnd1*.

(F–I′) Motor explants co-cultured with si*Plxnd1* or control HUVEC with or without VEGF^{Nab}. The fluorescent-secondary antibody used for VE-cadherin staining (red) also reveals VEGF in explants treated with VEGF^{Nab} due to matching host species of the primary antibodies (asterisks in G′ and I′).

(J–M′) Aberrant ingrowth of vessels into the MC (dashed lines) in *Plxnd1* mutants (K and K′, arrow) is rescued by conditional deletion of *Vegfa* in MNs with *Olig2^{MN}::Cre* (M and M′). *Plxnd1$^{-/-}$* embryos heterozygous for *Vegfa*-floxed allele are not rescued (L and L′, arrow).

(N) Quantification of vascular area (CD31^{+} px) within MCs. Control and *Plxnd1$^{-/-}$* measurements are also shown in Figure 3L. Mean, normalized to Ctrl ± SEM, ANOVA/Dunnett's test (***) $p < 0.00001$ *Plxnd1$^{-/-}$* and *Plxnd1$^{-/-}$*; *VEGF^{het}* versus *Ctrl*; (ns) $p > 0.1$ 0.1 *Plxnd1−/−*; *VEGFflox* versus *Ctrl*.

(O) Vascular invasion of *Plxnd1* mutants is rescued by *Vegfa* inactivation in MNs.

(P–S) Axon bundling (arrowheads) and epaxial nerve thinning (asterisks) distinctive of *Plxnd1* mutants are partially corrected by conditional deletion of *Vegfa* in MNs (E12.5 whole mounts, dorsal view).

(T) (Left) Quantification of axon guidance phenotype. Gradual rescue of *Plxnd1$^{-/-}$* axon defects by deletion of one (*Plxnd1$^{-/-}$*; *VEGFhet*) or two *VEGF* alleles (*Plxnd1$^{-/-}$; VEGF^{flox}*) in MNs. Mean ± SEM, ANOVA/Dunnett's multiple comparison test (***) $p < 0.0001$ *Plxnd1$^{-/-}$*; *VEGF^{het}* and *Plxnd1$^{-/-}$*; *VEGF^{flox}* versus *Plxnd1$^{-/-}$*. (Right) Penetrance and severity of phenotype in *Plxnd1/Vegfa* compound mutants compared with *Plxnd1$^{-/-}$*.

(U) Rescue of axon guidance errors of *Plxnd1* mutants by *Vegfa* gene inactivation in MNs.

(V) (Left) Interactions between motor axons and vessels in WT and *Plxnd1* mutant embryos (top). Dashed circles mark the choice point where epaxial MN axons use Sema3C/Plexin-D1 to displace meningeal ECs (EC^{Men}) that cross their path (bottom panels). Push-pull signals (including Sema3C and VEGF) prevent disruptive interactions and instruct alignment. Loss of EC repulsion in *Plxnd1* mutants results in unrestricted attraction to MNs and unmasks inhibitory vascular signals that obstruct axonal projection. In addition, vessels invade the MC. (Right) ECs detect Sema3C via Plexin-D1 in complex with NRPs. This repulsive pathway operates in parallel to VEGF/VEGFR2 attractive signaling. Conversely, ECs express both repellents and adhesive factors that signal to MNs.

Scale bars: 200 μm in (F)–(I′); 100 μm in (J)–(M′); and 100 μm in (P)–(S).

See also Figure S7.

KEY RESOURCES TABLE

REAGENT or RESOURCE	SOURCE	IDENTIFIER
Antibodies		
rabbit anti-Isl1/2	Ericson et al., 1992	N/A
rabbit anti-Hb9	Thaler et al., 1999	N/A
rabbit anti-GFP	Thermo Fisher Scientific	Cat# A-6455 RRID:AB_221570
mouse anti-GFP	Thermo Fisher Scientific	Cat# A-11120 RRID: AB_221568
chick anti-GFP	Abcam	Cat# ab13970 RRID:AB_300798
mouse anti-β3 tubulin	Abcam	Cat# ab7751 RRID:AB_306045
mouse anti-FLAG M2	Sigma-Aldrich	Cat# F1804 RRID:AB_262044
goat anti-Plexin-D1	R&D Systems	Cat# AF4160 RRID:AB_2237261
goat anti-VE-Cadherin	R&D Systems	Cat# AF938 RRID:AB_355726
rabbit anti-VE-Cadherin	Abcam	Cat# ab33168 RRID: AB_870662
rat anti-CD31	BD Biosciences	Cat# 550274 RRID:AB_393571
goat anti-CD31	R&D Systems	Cat# AF3628 RRID:AB_2161028
rabbit anti-Fsp1	Millipore	Cat# 07-2274 RRID:AB_10807552
rabbit anti-VAChT	Synaptic Systems	Cat# 139 103 RRID:AB_887864
rabbit anti-GAPDH	Cell Signaling Technology	Cat# 2118 RRID:AB_561053
rabbit anti-Pan-Actin	Cell Signaling Technology	Cat# 4968 RRID:AB_2313904
rat anti-Semaphorin3C	R&D Systems	Cat# MAB1728 RRID:AB_2301533
goat anti-NRP1	R&D Systems	Cat# AF566 RRID:AB_355445
goat anti-NRP2	R&D Systems	Cat# AF2215 RRID:AB_2155371
goat anti-VEGF164	R&D Systems	Cat# AF564 RRID:AB_2212821
donkey anti-goat IgG, Alexa Fluor 488	Thermo Fisher Scientific	Cat# A-11055 RRID:AB_2534102
donkey anti-goat IgG, Alexa Fluor 555	Thermo Fisher Scientific	Cat# A-21432 RRID:AB_2535853
donkey anti-goat IgG, Alexa Fluor 647	Thermo Fisher Scientific	Cat# A-21447 RRID:AB_2535864
donkey anti-mouse IgG, Alexa Fluor 488	Thermo Fisher Scientific	Cat# A-21202 RRID:AB_141607
donkey anti-mouse IgG, Alexa Fluor 555	Thermo Fisher Scientific	Cat# 31570 RRID:AB_2536180
donkey anti-mouse IgG, Alexa Fluor 647	Thermo Fisher Scientific	Cat# A-31571 RRID:AB_162542
donkey anti-rabbit IgG, Alexa Fluor 488	Thermo Fisher Scientific	Cat# A-21206 RRID:AB_2535792
donkey anti-rabbit IgG, Alexa Fluor 555	Thermo Fisher Scientific	Cat# A-31572 RRID:AB_162543
donkey anti-rabbit IgG, Alexa Fluor 647	Thermo Fisher Scientific	Cat# A-31573 RRID:AB_253618
goat anti-rat IgG, Alexa Fluor 546	Thermo Fisher Scientific	Cat# A-11081 RRID:AB_2534125
ChromPure Goat IgG, whole molecule	Jackson ImmunoResearch Labs	Cat# 005-000-003 RRID:AB_2336985
Chemicals, peptides, and recombinant proteins		
ENU, N-Ethyl-N-nitrosourea	Sigma-Aldrich	Cat# N3385
Laminin Mouse Protein	Gibco	Cat# #23017015
Fibronectin, human	Corning	Cat# 354008
Recombinant Human VEGF165	Miltenyi Biotec	Cat# 130-109-395
Recombinant Human GDNF	R&D Systems	Cat# 212-GD
Recombinant Mouse CXCL12/SDF-1 alpha	Prospec	Cat# CHM-324
Recombinant Human/Murine/Rat BDNF	Peprotech	Cat# 450-02

REAGENT or RESOURCE	SOURCE	IDENTIFIER
Recombinant Human Semaphorin 3C Fc	R&D Systems	Cat# 5570-S3
complete, EDTA-free Protease Inhibitor Cocktail	Merck/Roche	Cat# 04693132001
Halt Phosphatase Inhibitor Cocktail	Thermo Fisher Scientific	Cat# 78420
DharmaFECT4 transfection reagent	Dharmacon	Cat# T-2004-01
Lipofectamine 2000 Transfection Reagent	Thermo Fisher Scientific	Cat# 11668027
Trizol LS Reagent	Thermo Fisher Scientific	Cat# 10296010
Critical commercial assays		
Papain Dissociation System	Worthington Biochemical	Cat# LK003153
VECTASTAIN Elite ABC-HRP Kit, Peroxidase (Goat IgG)	Vector Laboratories	Cat# PK-6105
DAB Substrate Kit, Peroxidase (HRP)	Vector Laboratories	Cat# SK-4100
ClonExpress II One Step Cloning Kit	Vazyme	Cat# C112-01
GENEART Site-Directed Mutagenesis System	Thermo Fisher Scientific	Cat# A13282
M-MLV Reverse Transcriptase	Thermo Fisher Scientific	Cat# 28025013
Random Hexamers	Thermo Fisher Scientific	Cat# N8080127
SYBR Select Master Mix	Thermo Fisher Scientific	Cat# 4472913
T7 Quick High Yield RNA Synthesis Kit	New England Biolabs	Cat# E2050S
mMESSAGE mMACHINE™ T7 Transcription Kit	Thermo Fisher Scientific	Cat# AM1344
RNeasy Plus Mini kit	Qiagen	Cat# 74134
RNase-Free DNase Set	Qiagen	Cat# 79254
Illumina mRNA-Seq Sample Prep Kit	Illumina	Cat# RS-100-0801
TruSeq RNA Library Preparation Kit v2	Illumina	Cat# RS-122-2001
Deposited data		
RNA-seq data	This study	GEO: GSE207942
Experimental models: Cell lines		
HUVEC (Umbilical Vein Endothelial Cells)	Lonza	Cat# C2519A
AD-293	Stratagene	Cat# 240085
COS-7	ATCC	Cat# CRL-1651
NIH-3T3	ATCC	Cat# CRL-1658
Experimental models: Organisms/strains		
Mouse: *ISL^{MN}::fGFP*: *Tg(Isl1-EGFP*)1Slp/J*	Lewcock et al., 2007	JAX:017952
Mouse: *Olig2::Cre*	Dessaud et al., 2007	N/A
Mouse: *Hb9^{MN}::GFP*	Lee et al., 2004	N/A
Mouse: *MN$^{218\text{-}2)}$::GFP*	Amin et al., 2015	N/A
Mouse: *Tek::Cre* (Tie2::Cre)	Kisanuki et al., 2001	JAX:008863
Mouse: Kdr::Cherry (Flk1-myr::mCherry)	Larina et al., 2009	JAX:018542
Mouse: Plexin-D1 flox	Zhang et al., 2009	JAX:018319
Mouse: Plexin-D1 knockout	This study	N/A
Mouse: R26-DTA^{LSL} (Rosa26-DTA176)	Wu et al., 2006	JAX: 010527)
Mouse: Sema3C knockout	Feiner et al., 2001	N/A
Mouse: Sema3E knockout	Gu et al., 2005	N/A
Mouse: Sema4A knockout	This study	N/A

REAGENT or RESOURCE	SOURCE	IDENTIFIER
Mouse: VEGF^{flox}	Gerber et al., 1999	N/A
Oligonucleotides		
gRNA Sema4A #1 5'-TGGGGTGAGTAGCGGGCATAAGG	This study Guide RNA	N/A
gRNA Sema4A #2 5'- GCAGCGTGTCAAAGTCTCGGAGG	This study Guide RNA	N/A
Mouse Plexin-D1 C116S mutagenesis (forward primer) 5'-GCAGGCCTCGAGCGAGCAC	This study	N/A
Mouse Plexin-D1 C116S mutagenesis (reverse primer) 5'-GTGCTCGCTCGAGGCCTGC	This study	N/A
control siRNA (Non-targeting Pool)	Dharmacon	Cat#D-001810-10-05
Human PLXND1 (23129) siRNA SMARTpool	Dharmacon	Cat# L-014121-01-0005
Human NRP1 (8829) siRNA SMARTpool	Dharmacon	Cat# L-019484-00-0005
Human NRP2 (8828) siRNA SMARTpool	Dharmacon	Cat#L-017721-00-0005
Primers for quantitative RT-PCR	This study	Table S6
Recombinant DNA		
Plasmid: CMV-PlexinD1-FLAG	this study	N/A
Plasmid: CMV-PlexinD1-C116S-FLAG	this study	N/A
Plasmid: CMV-Plexin-D1-FLAG-P2A-Puro	this study	N/A
Plasmid: PiggyBac-CAG-NRP1-HA	this study	N/A
Plasmid: PiggyBac-CAG-NRP2-HA	this study	N/A
Plasmid: pCMV-HAhyPBase	Yusa et al., 2011	N/A
Plasmid: AP-Sema3E	Gu et al., 2005	N/A
Plasmid: AP-Sema3C	Chen et al., 1998	N/A
Plasmid: pN1-EGFP	Clontech	Addgene Cat# 6085-1
Plasmid for in situ probe: mouse Plxnd1 (GenBank: NM_026376; 3544-6913bp)	Gu et al., 2005	N/A
Plasmid for in situ probe: mouse Vegfa (GenBank: NM_001317041.1; 1431-1849bp)	Ruiz de Almodovar et al., 2011	N/A
Plasmid for in situ probe: mouse Sema3C (GenBank: NM_013657.5; 546-1441bp)	this study	N/A
Plasmid for in situ probe: mouse Sema3E (GenBank: NM_011348; 1130-1920bp)	this study	N/A
Software and algorithms		
STAR aligner	Dobin et al., 2013	RRID:SCR_004463
featureCounts	Liao et al., 2014	RRID:SCR_012919
ComBat	Zhang et al., 2020	RRID:SCR_010974
Bioconductor	Huber et al., 2015	RRID:SCR_006442
DESeq2	Love et al., 2014	RRID:SCR_015687
Enrichr	Xie et al., 2021	RRID:SCR_001575
GeneCodis	Tabas-Madrid et al., 2012	RRID:SCR_006943
UMI-tools	Smith et al., 2017	RRID:SCR_017048
SEURAT	Hao et al., 2021	RRID:SCR_007322
Expression Weighted Celltype Enrichment (EWCE)	Skene and Grant, 2016	https://doi.org/10.18129/B9.bioc.EWCE
CellPhoneDB	Efremova et al., 2020	RRID:SCR_017054
PROVEAN	Choi and Chan, 2015	RRID:SCR_002182

REAGENT or RESOURCE	SOURCE	IDENTIFIER
MOSAIK	Lee et al., 2014	RRID:SCR_005486
CRISPR Tool	Zhang Lab, MIT	http://crispr.mit.edu/
Fiji	http://fiji.sc	RRID:SCR_002285
ImageJ	https://imagej.net/	RRID:SCR_003070
Color Profiler (ImageJ plugin)	ImageJ	https://imagej.nih.gov/ij/plugins/color-profiler.html
FeatureJ (ImageJ plugin)	ImageJ	https://imagescience.org/meijering/software/featurej/
Adobe Photoshop	Adobe Systems Inc.	RRID:SCR_014199
Arivis Vision4D	Arivis-ZEISS	RRID:SCR_018000
GraphPad Prism	GraphPad Software, Inc	RRID:SCR_002798
Other		
Endothelial Cell Growth Basal Medium-2 (EBM-2)	Lonza	Cat# CC-3156
EGM-2 Endothelial factors	Lonza	Cat#CC-4176
RNA scope probe for mouse *Plxnd1*	ACD Bio-Techne	Cat# 405931
Alexa Fluor 488 Phalloidin	Thermo Fisher Scientific	Cat# A12379
Alexa Fluor 555 Phalloidin	Thermo Fisher Scientific	Cat# A34055
Hydrogel Solution	Logos Biosystems	Cat# C1310X
Electrophoretic Tissue Clearing Solution	Logos Biosystems	Cat# C13001
X-Clarity Mounting Solution	Logos Biosystems	Cat# C13101)